Published in final edited form as:
Bone. 2022 September ; 162: 116451. doi:10.1016/j.bone.2022.116451.

Alterations of bone material properties in growing *Ifitm5*/BRIL p.S42 knock-in mice, a new model for atypical type VI osteogenesis imperfecta

Ghazal Hedjazi[1,5], **Gali Guterman-Ram**[2], **Stéphane Blouin**[1,3], **Victoria Schemenz**[4,6], **Wolfgang Wagermaier**[4], **Peter Fratzl**[4], **Markus A. Hartmann**[1,3], **Jochen Zwerina**[1,3], **Nadja Fratzl-Zelman**[1,3,#], **Joan C. Marini**[2,#]

[1]Ludwig Boltzmann Institute of Osteology at the Hanusch Hospital of OEGK and AUVA Trauma Centre Meidling, 1st Medical Department Hanusch Hospital, Heinrich Collin Strasse 30, 1140 Vienna, Austria

[2]Section on Heritable Disorders of Bone and Extracellular Matrix, NICHD, NIH, Bethesda, USA

[3]Vienna Bone and Growth Center, Vienna, Austria

[4]Max Planck Institute of Colloids and Interfaces, Department of Biomaterials, Am Mühlenberg 1, 14476 Potsdam, Germany

[5]Present address: Lifebrain, 1140 Vienna, Austria

[6]Present address: Department of Operative and Preventive Dentistry, Charité-Universitätsmedizin - Berlin, Germany

Abstract

Introduction—Osteogenesis imperfecta (OI) is a heterogenous group of heritable connective tissue disorders characterized by high bone fragility due to low bone mass and impaired bone material properties. Atypical type VI OI is an extremely rare and severe form of bone dysplasia

---

Communicating author: Joan C Marini, MD, PhD, Head, Section on Heritable Disorders of Bone and Extracellular Matrix, NICHD, NIH, Bethesda, MD USA, 20892, oidoc@helix.nih.gov.

[#]= These authors made equal contribution

Authorship contribution statement:
Ghazal Hedjazi: conducted bone material experiments, formal analysis, data curation, writing original draft, review and editing
Gali Guterman-Ram: generation of mouse model, conducting experiments, writing: review and editing
Stéphane Blouin: Methodology, Formal analysis, Writing: review and editing
Victoria Schemenz: Formal analysis, Writing: review and editing
Wolfgang Wagermaier: Data curation: Writing: review and editing
Peter Fratzl: Data curation, formal analysis, Writing: review and editing
Markus A. Hartmann: Methodology, Data curation, Writing: review and editing
Jochen Zwerina: Data curation, Resources, Writing: review and editing
Nadja Fratzl-Zelman: Conceptualization, Methodology, Data curation, Writing: original draft, review and editing, visualization, supervision
Joan C. Marini: Conceptualization, Methodology, Data curation, Writing: original draft, review and editing, visualization, supervision.

Declaration of competing interest:
All authors state that they have no conflict of interest

resulting from a loss-of-function mutation (p.S40L) in *IFITM5/*BRIL, the causative gene of OI type V and decreased osteoblast secretion of pigment epithelium-derived factor (PEDF), as in OI type VI. It is not yet known which alterations at the material level might lead to such a severe phenotype. We therefore characterized bone tissue at the micrometer level in a novel heterozygous *Ifitm5/*BRIL p.S42L knock-in murine model at 4 and 8 weeks of age.

Methods: We evaluated in female mice, total body size, femoral and lumbar bone mineral density (BMD) by dual-energy X-ray absorptiometry. In the femoral bone we examined osteoid deposition by light microscopy, assessed bone histomorphometry and mineralization density distribution by quantitative backscattered electron imaging (qBEI). Osteocyte lacunae were examined by qBEI and the osteocyte lacuno-canalicular network by confocal laser scanning microscopy Vasculature was examined indirectly by qBEI as 2D porosity in cortex, and as 3D porosity by micro-CT in third trochanter. Collagen orientation was examined by second harmonic generation microscopy. Two-way ANOVA was used to discriminate the effect of age and genotype.

Results: *Ifitm5/*BRIL p.S42L female mice are viable, do not differ in body size, fat and lean mass from wild type (WT) littermates but have lower whole-body, lumbar and femoral BMD and multiple fractures.

The average and most frequent calcium concentration, CaMean and CaPeak, increased with age in metaphyseal and cortical bone in both genotypes and were always higher in *Ifitm5*/BRIL p.S42L than in WT, except CaMean in metaphysis at 4 weeks of age. The fraction of highly mineralized bone area, CaHigh, was also increased in *Ifitm5*/BRIL p.S42L metaphyseal bone at 8 weeks of age and at both ages in cortical bone. The fraction of lowly mineralized bone area, CaLow, decreased with age and was not higher in *Ifitm5*/BRIL p.S42L, consistent with lack of hyperosteoidosis on histological sections by visual exam. Osteocyte lacunae density was higher in *Ifitm5/*BRIL p.S42L than WT, whereas canalicular density was decreased. Indirect measurements of vascularity revealed a higher pore density at 4 weeks in cortical bone of *Ifitm5/*BRIL p.S42L than in WT and at both ages in the third trochanter. Importantly, the proportion of bone area with disordered collagen fibrils was highly increased in *Ifitm5/*BRIL p.S42L at both ages.

Conclusions: Despite normal skeletal growth and the lack of a collagen gene mutation, the *Ifitm5/*BRIL p.S42L mouse shows major OI-related bone tissue alterations such as hypermineralization of the matrix and elevated osteocyte porosity. Together with the disordered lacuno-canalicular network and the disordered collagen fibril orientation, these abnormalities likely contribute to overall bone fragility.

Keywords

osteogenesis imperfecta; growing mice; bone matrix mineralization; osteocyte lacunae; osteocyte canalicular network; bone vascularity; collagen orientation

---

Introduction:

Osteogenesis imperfecta (OI) or brittle bone disease is a rare heritable disorder of connective tissue characterized by low bone mass and high bone fragility [1, 2]. Patients with OI commonly manifest multiple fractures, skeletal deformities, and growth deficiency, all of which vary depending on the severity of the disease. The classical forms of OI originally described by Sillence encompass 80–85% of cases [3] and are due to autosomal dominant mutations in collagen type I encoding genes, *COL1A1* and *COL1A2* that lead to either quantitative or structural defects in collagen type I protein [4–6]. The resulting broad phenotypic spectrum varies from mild type I to moderate type IV, severe progressive deforming type III and perinatal lethal type II OI. More recently described, mostly recessive, forms of OI result from mutations in genes whose encoded proteins are involved in collagen post-translational modification, folding, or crosslinking, as well as osteoblast differentiation and matrix mineralization [7].

Types V and VI OI, first clinically described in 2000 and 2002, respectively, are both characterized by distinct defects in bone mineralization [8, 9]. Type V OI is a moderate form of OI resembling type IV OI in clinical severity, whereas type VI OI is severe-progressive-deforming, resembling type III OI in clinical severity [10, 11]. The autosomal dominantly inherited type V OI is caused by a recurrent heterozygous single nucleotide change (c.14C.T) in the 5´-UTR of the *IFITM5* gene encoding interferon induced transmembrane protein 5 (later called BRIL), leading to a gain-of-function through the N-terminal addition of 5 amino acids (MALEP-IFITM5), thus creating new start codon [10, 11]. Typical clinical features of type V OI are exuberant callus formation, which about 65% of patients develop after fracture or following corrective surgery, the ossification of the interosseous membrane of the forearms observed in nearly all affected individuals, as well as a dense metaphyseal band detected even in infancy [12, 13]. These unusual features may originate from dysregulated primary bone deposition by the periosteum. Indeed, in bone biopsy samples, a disordered, “mesh-like” lamellar structure was observed by polarized light microscopy, along with highly increased osteocyte lacunar density that is typical for rapidly laid-down immature bone and hypermineralization of the bone matrix [14]. In contrast to this, type VI OI is an autosomal recessive form caused by homozygous null mutations in *SERPINF1*, encoding pigment epithelium-derived factor (PEDF), a multifunctional glycoprotein and potent antiangiogenic factor expressed in many organs [15–18]. Under polarized light, the OI type VI bone matrix shows a disordered lamellar structure, described as “fish-scale pattern”, as well as excessive accumulation of unmineralized matrix or osteoid [9]. Moreover, the generalized lack of PEDF results in profound disturbance of mineralization with highly mineralized bone areas seamed by fringes with abnormally low mineral content and oddly shaped osteocyte lacunae surrounded by disordered, poorly mineralized fibrillar structures [19].

A physiological link between these two forms of OI first became evident in 2014 with the report of a very severe form of OI in a young woman carrying a *de novo* heterozygous point mutation in *IFITM5* p.Ser40Leu (S40L) [20]. The patient displayed some features typical of type VI OI, such as disordered “fish-scale” bone lamellar organization and prominent osteoidosis [20]. Her childhood serum alkaline phosphatase showed the marked elevation seen in type VI OI. Moreover, *in vitro* studies revealed a lack of PEDF secretion from differentiating osteoblasts and fibroblasts, although circulating PEDF levels were within normal range [20]. The functional connection between BRIL and PEDF was further confirmed by *in vitro* studies showing that osteoblasts from type V OI patients have increased levels of *SERPINF1* expression and PEDF secretion [21], reviewed by [7, 22].

This novel and unique form of OI, which was subsequently designated as “atypical OI type VI” has now been identified in 10 individuals [23, 24] (recently reviewed in [7]). The small number of patients increases the challenge of delineating the role of BRIL and PEDF in OI pathophysiology, as well as analyzing the effects on bone material properties.

OI types V and VI have not been extensively studied in murine models. A type V OI knock-in mouse model generated using Crispr/Cas9 technology did not recapitulate the human phenotype [25]. The mouse model was perinatally lethal and displayed severe skeletal defects such as bent and malformed long bones and hypomineralization of the skull [25]. In contrast to findings from primary osteoblasts derived from patients, murine derived cells show normal collagen production but delayed differentiation and mineralization [21, 26]. The *Serpinf1*$^{-/-}$ mouse is viable, reproduces some key features but does not mimic the severe type VI OI skeletal phenotype. It displayed defective mineralization along with altered expression of osteocyte specific genes regulating mineralization, increased mineral-to-matrix ratio, brittle bones and hypervascularization [27, 28]. To explore the metabolic pathway connecting BRIL and PEDF, an *Ifitm5/*BRIL p.S42L knock-in murine model of atypical OI type VI was recently generated [29]. Standard bone phenotype measures, as well as molecular and biochemical mechanisms will be described elsewhere (Guterman-Ram G. *et al.,* manuscript in preparation).

The aim of the present work is to characterize bone material properties at the micrometer scale during skeletal development in young *Ifitm5/*BRIL p.S42L knock-in mice and to compare the results to the well-known alterations in other forms of OI [18, 30–34]. While the patient has severe skeletal deformities and multiple fractures reminiscent of the clinical form of OI III [20], it is currently unknown whether and in which form the *Ifitm5/*BRIL p.S42 knock-in will actually affect the bone material properties of the skeleton. We therefore analyzed femoral bone from 4- and 8-week-old female mice, corresponding to pre-pubertal and pubertal stages, because some previously described OI murine models have their most severe phenotype at 2 months of age [35, 36]. Overall phenotype was characterized by monitoring body weight over age, as well as by DXA measurements. Quantitative backscattered electron imaging (qBEI) was used to measure bone mineralization density distribution (BMDD), histomorphometric parameters and characteristics of osteocyte lacunae, since osteocyte lacunae are increased in size and number in types V and VI OI bone [14, 37]. We further evaluated the osteocyte lacuno-canalicular network by confocal laser scanning microscopy (CLSM), for its potential contribution to bone mechanosensory function [38, 39]. Moreover, since dysregulation of PEDF secretion in type VI OI might alter bone vascularity [40], we evaluated this type of porosity in femoral bone and also in the 3rd trochanter. Finally, we quantified collagen fibril orientation by second harmonic generation (SHG) microscopy, given that extracellular matrix is highly disordered in types V and VI OI bone [8, 9, 14].

Material & Methods:

Animals

*Ifitm5/*BRIL p.S42L is a conditional knock-in (KI) murine model bred in a mixed Sv129/CD-1C57BL/6S background strain. It contains 2-point mutations in murine *Ifitm5/BRIL*

(Gene ID:73835; BLAST Protein NP_444318.1, c.125 C>T, c.126 T>G) that result in a p.Ser42Leu substitution. Murine BRIL p.Ser42 is the corresponding residue for human BRIL p.Ser40. The generation of the murine model and its more complete characterization will be described elsewhere (Guterman-Ram G et al., manuscript in preparation). The mutation was activated by crossing a conditional mouse with E2A-cre mice previously bred into a mixed background. All mice used for the experiments in this report were female. Mice were euthanized at 4 and 8 weeks of age using ketamine and xylazine. All protocols and procedures involving animals were conducted under an NICHD-ACUC approved protocol.

DXA analysis

Bone mineral density, femur area, body fat mass and body lean mass were assessed with dual-energy X-ray absorptiometry (DXA) on whole body, lumbar and left femur of 4- and 8-week-old female *Ifitm5* S42L and wild-type (WT) mice (n=18, n=26 and n=24, n=22, respectively), using a GE Lunar PIXImus2 (GE Healthcare, Chicago, IL) according to the manufacturer’s directions. Whole body measurement did not include the head. The DXA measurement of left femur and L3–4 vertebrae were done with ROI encompassing whole femur or both vertebrae, respectively. It should be noted that DXA was not systematically performed on the same set of animals that was used for microscopic material analyses.

Bone sample preparation and processing for the evaluation of bone material properties

10 animals for each genotype and age were chosen randomly for the evaluation of bone material properties. Left femurs of 4- and 8-week-old female *Ifitm5/*BRIL p.S42L and wild-types (WT) mice were analyzed for bone material properties. Figure 1 summarizes the methods applied in this study to characterize bone material properties, as well as their respective outcomes.

Femurs were fixed in 70% ethanol immediately after removal. The femurs were sectioned transversally, and the proximal part was analyzed by micro-CT (see below) and was subsequently stained with rhodamine for assessment of the osteocyte lacuno-canalicular network (see below). Both proximal and distal bone pieces were then separately dehydrated in graded series of ethanol (5 days in 70%, 80%, 96%, 100% and 100%, each). Subsequently the samples were defatted 2 days with acetone, then impregnated 2 days with pure polymethylmethacrylate and finally immersed in a mixture of polymethylmethacrylate and benzoyl peroxide allowing the hardening of the plastic. This procedure leads to plastic blocks containing the mineralized bone samples that can be sectioned in any direction since the plastic traps the bone tissue and prevent the collapse of the sample during the sawing/cutting/grinding and polishing processes as reported previously [34, 41, 42].

Rhodamine staining

For visualization of the osteocyte lacuno-canalicular network, the samples were stained with rhodamine prior embedding as described previously [43]. The procedure was performed using a mixture of ethanol and rhodamine (1.25 g rhodamine per 300 ml 100% ethanol). Samples were placed in tubes containing staining fluid (14 ml) for 3 days, with daily renewal of the staining fluid, on a homemade low speed spinning wheel, leading to a complete penetration with rhodamine of the sample [44, 45]. Eventually, embedding, and further preparation steps were performed.

Light microscopy

Polymethylmethacrylate embedded sample blocks from the distal femur were cut using a low-speed diamond saw (Isomet-R, Buehler Ltd. Lake Buff, IL, USA) to obtain longitudinal sections containing cortical and trabecular bone regions. For histological evaluations, 3 μm thin sections were cut from the tissue blocks using a hard tissue microtome (Leica SM2500, Nussloch, Germany). Subsequently the thin sections were de-plasticized using 2-methoxyethylacetate and stained with modified Goldner's Trichrome. The stained sections were investigated using a light microscope (Axiophot, Zeiss, Oberkochen, Germany) equipped with a digital camera (AxioCam HRc, Zeiss, Oberkochen, Germany).

Quantitative backscattered electron imaging (qBEI)

Sample preparation and qBEI measurements are described in detail elsewhere [34, 42, 46]. Briefly, the longitudinal surface of the residual sample block was ground and polished using a polishing device (PM5 Logitech, Glasgow, Scotland). To ensure electric conductivity the surface was carbon coated using vacuum evaporation (Agar SEM Carbon coater, Agar Scientific Limited, Essex, UK). Backscattered electron images were obtained using a digital scanning electron microscope (DSM 962, Zeiss, Oberkochen, Germany) equipped with a four-quadrant semiconductor backscattered electron detector. An accelerating voltage of 20 kV, a working distance of 15 mm and a probe current of 110 pA were used.

The underlying principle of the qBEI method is that the intensity of backscattered electrons from the surface is proportional to the local calcium content. A calibration of the electron microscope with standards of known composition (carbon and aluminum) prior to the measurements allows to convert local grey values into calcium concentration measured in weight % (wt% Ca).

Applying custom-made routines, different types of image analyses were performed on obtained quantitative backscattered electron microscopy images:

a) Structural histomorphometry of the mineralized bone tissue.—We performed structural histomorphometry on quantitative backscattered electron microscopy images with a spatial resolution of 3.6 μm per pixel. Of note, it was previously shown that shrinkage of mineralized bone due to dehydration during sample preparation is minimal and homogeneous, given that structural parameters obtained from 3D micro-CT and 2D-histomorphometry performed on plastic embedded tissue are in excellent agreement [47]. The measurement area extended 1 mm towards the midshaft of the bone, starting 0.5 mm below the growth plate. The following parameters were assessed by standardized procedures [48]

- BV/TV (%), i.e, bone volume per tissue volume,
- Tb.Th (μm), i.e., trabecular thickness,
- Tb.N (1/mm), i.e., trabecular number,

It is important to note that in contrast to histomorphometry on Goldneŕs stained sections, the parameters obtained in this evaluation reflect only the mineralized parts of bone and do not include any unmineralized matrix (osteoid).

b) Bone Mineralization Density distribution (BMDD)—The cortical (cort) and metaphyseal (ms) part of distal femurs were scanned with a spatial resolution of 0.88 µm per pixel and a scan speed of 100 s per frame. From the quantitative backscattered electron microscopy image showing the mineral content in each pixel, the corresponding frequency distribution, called bone mineralization density distribution (BMDD), is derived. This enables direct comparison of the mineralization pattern expressed by the specific BMDD curve between different bone samples. The BMDD curve is characterized by five parameters [46].

- CaMean (wt% Ca); the average calcium concentration,
- CaPeak (wt% Ca); the most frequently measured calcium concentration,
- CaWidth (Δwt% Ca); the full width at half maximum of the curve, characterizing the heterogeneity in matrix mineralization,
- CaLow (% bone area); the percentage of lowly mineralized bone defined as the area below 17.68 wt% calcium). This cut-off corresponds to the 5th percentile of the reference range BMDD in human adults. As previously described, this value mirrors the transition of the phase of primary to secondary mineralization [42, 46].
- CaHigh (% bone area); the percentage of highly mineralized bone area, which is mineralized above the 95th percentile of the WT BMDD curve as described previously [42]. The mineralization values of the 95th percentile for WT animals were defined from the BMDDs from WT for each age and each femoral region as follow: at age of 4 weeks: 28.24 wt% Ca (ms); 27.03 wt% Ca (cort); at age of 8 weeks: 28.42 wt% Ca (ms) 28.94 wt% Ca (cort).

c) Osteocyte lacunae section (OLS) characteristics—The analysis of osteocyte lacunae sections was performed on quantitative backscattered electron microscopy images with 0.88 µm pixel resolution using a custom-made macro in ImageJ (version 1.50f; NIH, Bethesda, MD, USA; https://imagej.nih.gov/ij/) [49]. The images were binarized using a threshold of 5.2 wt% Ca to discriminate mineralized bone matrix from OLS. The OLS were further filtered using a size threshold between 5 μm^2 and 80 μm^2 to distinguish them from vascular channels or cracks [14].

The OLS characteristics are described by four parameters.

- OLS-porosity (%); defined as the OLS total area per bone area,
- OLS-density (OLS number/mm^2); defined as the number of OLS per bone area,
- OLS-area (μm^2); mean value of the OLS area per sample,
- OLS-perimeter (µm); mean value of the OLS perimeter per sample,

The remaining analyses (except micro-CT) were performed on cross-sections of proximal femoral bone.

d) Indirect measurement of 2D vascular porosity—2D vascularity was investigated on quantitative backscattered electron microscopy images with a resolution of 2.97 µm per pixel. All entities larger than a size threshold of 80 µm^2 were defined as being presumptively vascular pores.

Further, vascular variables were measured and expressed as:

- Vascular porosity (%); described as total vascular pore area per bone area,
- Vascular density (vascular pore number/mm^2); described as the number of vascular pores per area total bone area,
- Vascular mean area (µm^2); mean value of the vascular pore area per bone area.

Characterization of the Osteocyte Lacuno-canalicular Network

The osteocyte lacuno-canalicular network of rhodamine-stained samples was visualized by confocal laser scanning microscopy (CLSM, TCS SP5, Leica, Wetzlar, Germany). An oil-immersion objective (HCXPL APO 63x/140–60 OIL) with an airy 1 pinhole of 95.5 µm was used. The measurements were done on three regions of interest (ROI): anterior (ROI1), medial (ROI2), posterior (ROI3), in the midshaft cross-section of the proximal part of the left femur. For each region we obtained image stacks of 1024×1024 pixels with lateral resolution 0.24 µm/pixel and a step size of 0.25 µm in z-direction reaching to a depth of approximately 60 µm in the sample. Images were obtained with a 543 nm laser. The laser intensity and the photomultiplier gain voltage were adjusted continuously in depth to guarantee a sufficient image quality. The images were analyzed using the TINA software package developed by F. Repp and co-workers [43]. TINA is a collection of Python scripts to binarize, skeletonize and analyze the obtained images. The main result of the analysis is the osteocyte lacuna-canalicular density measured as total canalicular length per volume and expressed as m/mm^3 corresponding to 10^{-3}µm/µm^3 [43]. We also characterized the degree of osteocytes, i.e., the number of canaliculi emanating from each osteocyte lacuna. In addition, the relation between osteocyte lacuna degree and the osteocyte volume was tested.

X-ray microcomputed tomography (micro-CT)

Micro-CT was used to assess vascular porosity in the third trochanter of the femur, a standardized region with a well-defined 3D-structure. For measurements, the proximal part of the femurs was immersed in 70% ethanol. The specimens were vertically positioned and fixed in the sample holder to prevent any motion artifacts during measurement [50]. We used a micro-CT50 (Scanco Medical AG, Brüttisellen, Switzerland) operated at 55 kV and 200 µA. A 0.5 mm thick aluminum filter was used, and the exposure time was 1215 ms per projection. A total of 1500 projections were captured over the range of 180 degrees. Images with 2 µm spatial resolution were obtained after data reconstruction. The obtained images were processed with ImageJ (https://imagej.nih.gov/ij/). A 3D median filter with 2-pixel radius and a 3D gauss filter of 3-pixel size was applied to reduce noise. Image segmentation using a local Phansalkar threshold with radius 50 pixels and k= 0.15 was applied. The porosity (%) shown as (PV/TV), pore surface (μm^{-1}) (PS/TV), pore thickness (µm) (P.Th), pore separation (µm) (P.Sp), pore number (μm^{-1}) (P.N) were assessed with the plugin BoneJ [51] with a minimum pore size threshold set at 4000 μm^3. The 3D structure of the pores was rendered using Amira software (v6.5, FEI Visualization Sciences Group, Bordeaux, France). The height of the third trochanter, was about 1.9 mm in the 4-weeks-old mice, and 3.2 mm for the 8-weeks-old mice.

Second Harmonic Generation microscopy (SHG)

Second harmonic generation (SHG) microscopy was used to assess the orientation of collagen fibers in the bone matrix [52, 53]. The analysis was done on total midshaft cross-sections of the left femur. A two-photon confocal laser scanning microscope (Leica TCS-SP8 CLSM, Wetzlar, Germany) equipped with a pulsed IR-laser with 910 nm excitation wavelength was used. The laser power at the specimen surface was approximately 650 mW. Images of 1024×1024 pixels were obtained from the polished bone samples using an oil-immersion objective lens with nominal magnification 63x resulting in a pixel resolution of 0.18 µm. The signal emissions were collected in the spectral window between 450 nm and 460 nm. A frame average of 8 was applied to reduce the noise [34]. The .tiff images were transferred into ImageJ and subsequently an auto-threshold was applied to discriminate collagen from dark background. The different regions of the images were then assessed visually and distinguished manually into areas with highly aligned collagen and areas of disordered collagen fibrils using a computer drawing pen. The respective areas were then quantified using dedicated tools in ImageJ. Putting these areas in relation to the total area of the bone section yielded the respective percentages (shown in Figure 9A, B).

Statistical analysis

We performed two-way ANOVA analyses to test the effect of genotype and age of each variable. This was followed up by Tukey post-hoc tests to compare groups whenever the interaction term was significant. The results from two-way ANOVA analyses are compiled in Table 1.

On graphs, the data are presented as box-whiskers-plots. The horizontal line shows the median value, the cross indicates the mean value. The box extends from the 25th to the 75th percentile, the length of the whiskers indicate datás minimum and maximum. Differences were considered statistically significant at $p<0.05$. The significance based on two-way ANOVA analyses is shown using § and * symbols for main effect of age and main effect of genotype, respectively, when the interaction term was non-significant (with $p < 0.05$, $p < 0.01$, $p < 0.001$ for one, two and three symbols, respectively). When the interaction term was significant, the results of the post-hoc tests are given with pairwise comparisons when $p < 0.05$. All results of two-way ANOVA analyses are compiled in Table 1.

The relation between lacuna degree and osteocyte volume was tested by Pearson correlation. For all analyses GraphPad Prism was used (version 9.0, GraphPad Software, Inc., La Jolla, CA, USA).

Results:

Female *Ifitm5*/BRIL p.S42L mice have normal body weight, normal fat and lean mass but DXA BMD is reduced

Female mutant mice did not differ from WT in body weight and size at 4- and 8-weeks of age. X-ray analysis showed humeral fractures in 6 out of 14 animals at 4 weeks of age and in 9 out of 24 mice at 8 weeks of age (Figure 2 A, B, C).

Two-way ANOVA results are compiled in Table 1 and Figure 2D. The analyses showed that there was no effect of genotype for femur area, body fat and lean mass as measured by DXA. In contrast, there was a significant effect of genotype for BMD: *Ifitm5*/BRIL p.S42L mice had reduced BMD compared to WT, (whole body BMD: −9.3%, −5.7%; femoral BMD: −12.0%, −5.3%; lumbar spine BMD: −13.0%, −5.3%, respectively at 4 and 8 weeks of age)

There was also a significant effect for age for all DXA measures that increased between 4 and 8 weeks of age: femur area BMD (WT: +9.7%, *Ifitm5*/BRIL p.S42L: +8.8%), body fat mass (WT: +15.9%, *Ifitm5*/BRIL p.S42L: +21.6%), body lean mass (WT: +9.9 %, *Ifitm5*/BRIL p.S42L: +12.2%), whole body BMD (WT: +37.7%, *Ifitm5*/BRIL p.S42L: +43.3%), femur BMD (WT: +31.8%, *Ifitm5*/BRIL p.S42L: +41.8%), lumbar BMD (WT: +61.7%; *Ifitm5*/BRIL p.S42L: +77.0%) (Figure 2D, Table 1).

Trabecular architecture in femoral bone is similar in female *Ifitm5*/BRIL p.S42L and WT mice:

The region of interest for evaluations is shown in Figure 3A. The results of the two-way ANOVA analyses are compiled in Figure 3B and Table 1 and do not show any genotype-dependency for bone volume per tissue volume (BV/TV), trabecular thickness (Tb.Th) and trabecular number (Tb.N)

In contrast, Tb.N and Tb.Th showed a significant age dependency: Tb.N decreased with age (WT: −32.1%; *Ifitm5*/BRIL p.S42L: −28.0%), while Tb.Th increased between 4 and 8 weeks of age (WT: +21.2%; *Ifitm5*/BRIL p.S42L: +23.2%). As a consequence, BV/TV did not show a significant variation with age.

Goldner stained histological sections of *Ifitm5*/BRIL *p.S42L* and WT femoral bone were examined by light microscopy (Figure 4). Although quantitative bone histomorphometry was not performed, there was no obvious excessive osteoid deposition in *Ifitm5*/BRIL p.S42L bone samples. This observation is in agreement with the lack of increase of lowly mineralized matrix (CaLow) observed by qBEI (see Table 1, Figure 5 C).

Bone matrix mineralization is increased in female *Ifitm5*/BRIL p.S42L femora

We evaluated two regions of interest: the metaphyseal spongiosa (ms) and the midshaft cortical (cort) bone (Figure 5A). Typical BMDD curves for 4 and 8-week-old mice are shown in Figure 5B. In the younger age group, we observed in both genotypes, a high mineralization “shoulder” at the right side of the BMDD curves of metaphyseal spongiosa, indicative for residual mineralized cartilage (red arrow) [42]. At 8 weeks of age, the BMDD curves are shifted to the right, towards higher mineral content of the matrix compared to the corresponding BMDD from 4 weeks old mice. Moreover, at both ages, at both bone sites, the BMDD curves from *Ifitm5/*BRIL p.S42L are shifted toward higher mineral densities compared to the corresponding BMDD from WT mice. These observations were further confirmed by our two-way ANOVA analyses showing a significant effect for age and genotype for most BMDD parameters (Figure 5C, and Table 1).

In metaphyseal bone, the mean and peak calcium contents were higher in *Ifitm5/*BRIL p.S42L than WT (CaMean: +0.3% and +3.7%, CaPeak: +1.7% and + 3.4% for 4 and 8 weeks of age, respectively). Nevertheless, a post-hoc test performed due to a significant interaction term revealed that for CaMean only the 8 weeks difference was significant (4 weeks: p=0.9; 8 weeks: **P=0.004**). There was also a significant effect of genotype for the fraction of highly mineralized bone area, CaHigh. Post-hoc showed that CaHigh was significantly increased in *Ifitm5/*BRIL p.S42L vs. WT at 8 weeks (+98.6%, **P=0.003**) but not at 4 weeks (*Ifitm5/*BRIL p.S42L vs. WT +5.6%, P=0.99). There was no significant effect of genotype for either the heterogeneity in mineralization, CaWidth, or the fraction of lowly mineralized bone area, CaLow.

We further noted a highly significant age-dependency for all BMDD parameters except for CaHigh In particular, CaMean and CaPeak increased between 4 and 8 weeks of age (CaMean: WT: +5.7%, *Ifitm5/*BRIL p.S42L: +9.3%, both **P< 0.0001**; CaPeak: WT: +7.8%, *Ifitm5/*BRIL p.S42L: +9.5%) while CaWidth decreased (WT: −18.6%, *Ifitm5*/BRIL p.S42L: −17.2%) with age. Post-hoc tests for CaLow (due to a significant interaction) showed a decrease with age in both genotypes (WT: −20.5%, **P=0.01** and *Ifitm5/*BRIL p.S42L: −35.6%, **P<0.0001**).

In cortical bone, all BMDD parameters showed a significant genotype dependency. The mineral content of the matrix was higher in *Ifitm5/*BRIL p.S42L than in WT at 4 weeks (CaMean: +4.9%, CaPeak: +5.7%, CaHigh: +265%;) and at 8 weeks of age (CaMean: +4.1%, CaPeak: +4.2%, CaHigh: +272.0%). Also, CaWidth was increased in *Ifitm5*/BRIL p.S42L vs. WT (+11.4% and +6.9%, at 4 and 8 weeks of age, respectively). CaLow showed only a marginally significant difference with respect to genotype (P< 0.0490) and was decreased in *Ifitm5*/BRIL p.S42L vs. WT (−9.3% and −4.9%, at 4 and 8 weeks of age, respectively).

Moreover, the mineral content of the matrix increased with age in both genotypes reflected by an increase in CaMean (WT: +8.9%, *Ifitm5/*BRIL *p.* S42L: +8.0%) and CaPeak (WT: +8.4%, *Ifitm5/*BRIL p.S42L: +6.9%) between 4 and 8 weeks of age, whereas there was a decrease in CaWidth (WT: −2.9%; *Ifitm5/*BRIL p.S42L: −6.8%) and CaLow (WT: −38.1%, *Ifitm5/*BRIL p.S42L: −35.0%). CaHigh was the only BMDD parameter showing no significant alteration with age.

Osteocyte lacunae density is increased but size is reduced in female *Ifitm5*/BRIL p.S42L:

Figure 6 A shows typical backscattered images from femoral mid-shaft regions from wild type and *Ifitm5/*BRIL p.S42L mice used to evaluate the characteristics of osteocyte lacunae sections (OLS). The results of the two-way ANOVA analyses are compiled in Table1 and reveal a significant effect of age and genotype on all parameters.

As shown in Figure 6B, *Ifitm5/*BRIL p.S42L mice have at both ages higher OLS-porosity (+20.8% and +6.4% at 4 and 8 weeks of age, respectively), OLS-density (+40.1% and +23.7% at 4 and 8 weeks of age, respectively), smaller OLS-area (−13.8% and −14.0% at 4 and 8 weeks of age, respectively), and smaller OLS-perimeter (−7.5% and −7.3% at 4 and 8 weeks of age, respectively).

In both genotypes, OLS-porosity decreased with age (WT: −40.1%, *Ifitm5/*BRIL p.S42L: −48.0%). This was due to a concomitant decrease of OLS-density (WT: −27.2%; *Ifitm5/*BRIL p.S42L: −35.7%) and size (OLS-area: WT: −20.0%, *Ifitm5/*BRIL p.S42L: −20.2% and OLS-perimeter: WT: −8.4%, *Ifitm5/*BRIL p.S42L: −8.1%).

Osteocyte canalicular density is decreased in female *Ifitm5*/BRIL p.S42L:

We measured the osteocyte canalicular density, i.e., the total length of canaliculi per bone volume and the number of canaliculi emerging per osteocyte lacunae (degree of the lacunae) in three regions of interest (ROI) using confocal laser scanning microscopy. Representative images are shown in Figure 7A and 7B.

Two-way ANOVA analyses revealed an effect of age and genotype. Canalicular density increased with age in both genotypes (WT: +3.7%, *Ifitm5/*BRIL p.S42L: +11.8%). However, at both ages we observed significantly lower canalicular densities in *Ifitm5*/BRIL p.S42L vs. WT (−13.9% and −7.2%, at 4 and 8 weeks, respectively; data shown in Figure 7C and Table 1).

We further assessed the average number of canaliculi emanating from each osteocyte lacuna (lacunar degree). 2-way ANOVA revealed no effect of genotype between *Ifitm5/*BRIL p.S42L and WT mice in either age group, but a significant increase in number of canaliculi per osteocyte with age (WT: +29.8%, *Ifitm5/*BRIL p.S42L: +36.6%, respectively between 4 and 8 weeks of age; Figure 7D and Table 1). In addition, we performed Pearson correlations and found a strong positive correlation between osteocyte lacunae volume and the number of canaliculi emanating from it in both age groups for both genotypes (at both ages, r = 0.8 for WT and 0.7 for *Ifitm5/*BRIL p.S42L, all **p<0.0001**, Figure 7 E).

Vascular pore density is elevated in female *Ifitm5*/BRIL p.S42L:

We examined 2D vascularity by quantitative backscattered electron microscopy imaging on the cross-sectioned area of cortical bone diaphysis of femoral bone (Fig 8A) and 3D vascularity of the 3rd trochanter by micro-CT (Fig 8B). Both modalities showed decreased vascularity with age and increased measures of vascularity in 4-week-old *Ifitm5/*BRIL p.S42L mice vs WT (Figure 8 C, 8D). The results of the two-way ANOVA analyses are compiled in Table 1.

Two-way ANOVA analysis of vascularity showed that 2D porosity and 2D density have a significant effect of age and genotype. At both ages 2D-vascular porosity was increased in *Ifitm5/*BRIL p.S42L vs. WT (+96.3%, +12.9 % at 4 and 8 weeks, respectively). The relative higher porosity in *Ifitm5/*BRIL p.S42L at 4 weeks of age was due to a higher pore density at 4 weeks (+76.3% vs. WT, **P<0.001** from a post-hoc test due to a significant interaction), whereas there was no significant difference at 8 weeks of age (P=0.96). There was no significant genotype effect for 2D-pore area. Thus, pore area differed in the 4- and 8-weeks old mice in the same way regardless of genotype.

Both genotypes, showed an age-related decrease in 2D-porosity (WT: −74.8%, *Ifitm5/*BRIL p.S42L: −85.5%), 2D-density (WT: −60.3.8%, *Ifitm5/*BRIL p.S42L: −736%) and 2D-mean area (WT: −51.2 %, *Ifitm5/*BRIL p.S42L: −45.5%; Figure 8C).

Two-way ANOVA analysis from 3D pore evaluation in the third trochanter, showed a significant effect of age and genotype for pore number (P.N) and pore separation (P. Sp). In both genotypes P.N decreased between 4 and 8 weeks of age (WT: −27.7%, *Ifitm5/*BRIL p.S42L: −32.3%) but was always higher in *Ifitm5/*BRIL p.S42L than WT (4 weeks: +10.8%, 8 weeks: +3.7%). Consistently, P.Sp increased with age in both genotypes (WT: +44.7%, *Ifitm5/*BRIL p.S42L: +50.3%) and was lower in *Ifitm5/*BRIL p.S42L than WT (4 weeks: −7.7%, 8 weeks: −4.3%; results shown in Table 1 and supplemental Table). Pore volume and pore surface also decreased from 4- to 8- weeks of age in both genotypes (PV/TV: WT: −59.5%, *Ifitm5/*BRIL p.S42L: −59.7%; PS/TV: WT: −55.6%, *Ifitm5/*BRIL p.S42L: −59.7%), whereas pore thickness (P.Th.) increased with age (WT: +28.6%; *Ifitm5/*BRIL p.S42L: +44.9%). There was no significant effect of genotype for PV/TV, P.Th. and PS/TV. Thus, pore volume, pore thickness and pore surface differed in the 4- and 8-weeks old mice in the same way regardless of genotype (Figure 8D).

Collagen fibril orientation is highly disordered in female *Ifitm5*/BRIL p.S42L mice:

Collagen fibril orientation was examined by second harmonic generation (SHG) imaging. Representative images are shown in Figure 9A. A significantly higher area fraction from the total bone cross-section corresponding to disordered collagen fibrils was found in *Ifitm5/*BRIL p.S42L mice vs. WT (Figure 9B). This observation was confirmed by two-way ANOVA analyses presented in Figure 9C and Table 1, showing a significant effect of genotype but no significant effect of age. At both ages the proportion of disordered collagen fibrils was increased in *Ifitm5/*BRIL p.S42L versus WT (4 weeks: +155.3%, 8 weeks: +170.9%).

The relation between collagen orientation and osteocyte canalicular density results is further illustrated by Figure 10C, representing the overlay image from the same cortical bone region measured with SHG (Figure 10A) and CLSM (Figure 10B), which shows that the areas with ordered lamellar bone correspond to the regions with higher osteocyte canalicular density.

Discussion:

In the present study, we characterized the bone phenotype and material properties of femoral bone in young growing female 4- and 8-weeks old mice carrying an *Ifitm5/*BRIL p.S42L substitution, which is a new murine model for atypical type VI OI. The age of 4 weeks (and through 8 weeks) in mice corresponds to a period of rapid bone acquisition, which was similar in WT and in mice carrying the *Ifitm5/*BRIL p.S42L mutations as demonstrated by our growth curves and body weight analyses. Consistently, structural bone histomorphometry parameters from femoral bone obtained by qBEI, showed similar trabecular bone architecture in *Ifitm5/*BRIL p.S42L and WT. In particular, we observed between 4 and 8 weeks of age, in both genotypes a reduction in trabecular number and concomitant increase in trabecular thickness resulting in a constant trabecular bone volume (BV/TV). Such age-related changes are possibly driven by bone modeling and remodeling activities, resulting in structural adaptation to mechanical loading conditions during skeletal growth [36, 42]. This lack of skeletal growth anomalies contrasts with the perinatal lethality of mice harboring the recurrent OI type V mutation (14C>T, or MALEP-*Ifitm5*), which is the most common mutation. Furthermore, the murine *Ifitm5/*BRIL p.S42L phenotype is less severe in mice than in humans in terms of growth but does have spontaneous fractures [20, 25]. In addition, we did not observe by light microscopy examinations an obvious mineralization defect with excessive osteoid accumulation, as in patients with typical and atypical OI type VI [9, 20]. Although we did not obtain quantitative measures for osteoid, our observation is consistent with the qBEI results that did not show in *Ifitm5/*BRIL p.S42L an increase in CaLow, the percentage of lowly mineralized bone matrix, as one would expect in situation of hyperosteoidosis such as in OI type VI bone (Figure 5C) [19, 46].

Despite the similarity in body size, lean and fat mass, geometry and histology, the *Ifitm5/*BRIL p.S42L mouse cohort displayed multiple long-bone fractures and reduced whole body BMD, indicating bone material alterations at the microscopic scale. Consistently, detailed qBEI, micro-CT, confocal laser scanning and second harmonic generation microscopy analyses showed an array of OI bone tissue abnormalities associated with various OI types, which were: hypermineralization of the bone matrix, elevated vascular porosity, increased osteocyte lacunae density, decreased osteocyte canalicular density and highly disordered collagen orientation.

So far, elevated matrix mineralization was reported in children with OI and in all mouse models with genetic defects altering either the quantity or the structure of type I procollagen, and also with many OI types caused by deficiency of proteins affecting collagen modification, folding or processing, such as in the OI type VII and VIII murine models and even in OI type V and type VI, which do not affect modification, folding/processing [2, 9, 14, 19, 27, 33, 41, 42, 54–58]. In this study, we observed that the degree of mineralization (CaMean and CaPeak) increased with age in the metaphysis and in the cortical compartments, independently of genotype, and was always higher in *Ifitm5/*BRIL p.S42L than in WT. It should be noted that due to higher remodeling rate, the metaphyseal trabecular bone has an overall younger tissue age than cortical bone, and therefore, also a lower mineral content. This was reflected by lower CaMean and CaPeak values in metaphyseal than in cortical bone. We further noted, in the metaphyseal bone of 4-weeks old animals, a “shoulder” (see Figure 5B) in the BMDD peak at high mineralization. Such highly mineralized areas in metaphyseal bone of young mice represent remnants of mineralized cartilage from the growth plate, which is typically more highly mineralized than bone and make a substantial contribution to CaHigh [42]. However, CaHigh was significantly increased in metaphyseal bone of 8-weeks old *Ifitm5/*BRIL p.S42L versus WT mice, although no mineralized cartilage (or “shoulder” of the BMDD peak) was observed at this age. Moreover, in cortical bone, CaHigh was about 4 times higher in *Ifitm5/*

BRIL p.S42L than in WT. Thus, CaHigh, together with the marked increase of CaMean and CaPeak, mirrors the hypermineralization of the matrix, which is considered to be an important contribution to the increased material brittleness typical for OI bone [41, 59].

A further important finding is that intracortical porosity, encompassing vascular channels and osteocyte lacunae, decreased markedly with age in *Ifitm5/*BRIL p.S42L as well as in WT and was consistently higher in *Ifitm5/*BRIL p.S42L than in WT. While we applied an indirect method to evaluate vascular porosity in the cortex based on 2D backscattered electron microscopy images, a previous study on mouse bone has demonstrated the presence of blood vessels within large pores corresponding to intracortical channels [40]. The increased porosity is in accordance with the lower BMD obtained by DXA in *Ifitm5/*BRIL p.S42L versus WT in femoral bone (and lumbar spine) and might significantly undermine bone material strength and its ability to resist fractures [30, 60].

It is noteworthy that increased vascularity is generally not considered to be a typical feature of OI, although abnormally high number of vascular channels was previously demonstrated in diaphyseal bone of children with mild and severe forms of OI as well as, in the *oim* mouse model , which makes an atypical $\alpha 1(I)_3$ collagen [40, 61]. Moreover, PEDF has potent anti-angiogenic properties, manifest in the increased vascularity that was recently demonstrated directly by perfusion in a KO PEDF mouse model of type VI OI [28]. Reduced expression and secretion of PEDF was previously demonstrated in osteoblasts from patients with atypical type VI OI, leading to the expectation that vascular porosity might be increased in *Ifitm5/*BRIL p.S42L bone [20]. In fact, the increased porosity in *Ifitm5/*BRIL p.S42L bone was mainly due to increased pore density (pore number) as evaluated on 2D qBEI images and 3D rendering of the third trochanter (in agreement with a smaller pore spacing). Indeed, the 2-way ANOVA analysis did not reveal a significant effect of genotype either for the pore mean area on qBEI images or for pore volume, pore thickness and pore surface in the third trochanter (Table 1). These results are in line with previous findings in the *oim* mouse and might reflect a more disordered architecture such as smaller and more branched vascular channels [40].

Moreover, we noted that 2D pore density which was higher in *Ifitm5/*BRIL p.S42L at 4 weeks reached similar values than WT at 8 weeks of age (2-wayANOVA indicating a significant interaction between age and genotype, Figure 8C, Table1). Also the mean area of the pores showed a strong decrease with age (Figure 8C, Table1) Murine cortical bone is known to be highly vascularized at birth and early skeletal growth is accompanied by a steep decrease in porosity, estimated to be as much as 8-fold during the first 40 days of life [62–64]. This is related to the fact that limb bones are originally formed as a foamy, well-perfused but only partly mineralized scaffold, that gradually undergoes compaction due to a decrease of pore density and size [63, 65]. Hence, the decrease in pore density is due to apposition of more compact bone tissue at the inner and outer surfaces leading to radial expansion of the cortex. The gradual reduction of pore diameter is associated with activity of bone forming osteoblasts transported by blood vessels [63, 64]. Consistently, our analyses revealed that the age-related decrease in porosity was due to a concomitant decrease in pore density and pore size (area and perimeter) (Figure 8). Previous studies have found that the vascular canal diameter in murine cortical bone decreased from 32±3.3μm at 10 days of age to 15±15μm at 8 weeks [40, 63], which is in good agreement with our observations of a diameter decrease in WT from about 33μm to 23μm (Supplemental Table). Direct examination of vasculature in *Ifitm5/*BRIL p.S42L bone by perfusion in the future will be useful to validate the pore measurement data for bone angiogenesis.

In line with the qBEI findings in the cross-sectional area of the mid-diaphyseal cortical bone, our micro-CT analysis of the third trochanter showed that pore volume, pore surface and pore number significantly decreased with age, whereas 2 way-ANOVA indicated that pore number were increased in *Ifitm5/*BRIL p.S42L, regardless age (Figure 8D, Supplemental Table). It should be noted that the third trochanter, to which the ascending tendon of the gluteus maximus muscle attaches, is very likely to be subjected to different mechanical stress than the whole femoral bone, which might explain the different channel architecture [66, 67]. Nevertheless, there is a strong indication that angiogenesis was increased in female *Ifitm5/*BRIL p.S42L at the age of 4 weeks and normalized thereafter (Figure 8D). Of note, it has been previously reported that conditional disruption of VEGF in mature osteoblasts increases blood vessel formation in males but does not alter vascular porosity in adult female mice [68]. Because estrogen bioactivity peaks at 8 weeks of age, which in fact corresponds to a state of late puberty in mice, it might be that the *Ifitm5/*BRIL p.S42L mutation is compensated in female mice by other, still unknown angiogenic factors [36, 68, 69].

In both murine genotypes, osteocyte lacunae sections (OLS) porosity and OLS density, measured on quantitative backscattered electron microscopy images, decreased from 4 weeks to 8 weeks of age and was higher in *Ifitm5*/BRIL p.S42L than in WT (Figure 6B). Elevated osteocyte density is a hallmark of OI bone and was also observed in several murine OI models. It has been associated with a higher bone turnover rate and abnormally low bone formation capacity by individual OI osteoblasts [14, 30, 40, 70–73]. Indeed, a greater osteocyte density indicates that less matrix per osteocyte is present in OI bone which points towards disturbed osteoblast and osteocyte differentiation and function in OI pathology with and without primary collagen defect [14, 18, 30, 40, 70–74]. Consistent with the present findings, a decrease in osteocyte lacunar density with age has been previously observed in bone from children with or without OI [70, 75]. Moreover, as in *Ifitm5/*BRIL p.S42L mutants, a significantly smaller OLS size was also observed in transiliac bone biopsy samples from children with type I OI, whereas children with type V OI, and to a certain extent also children with OI type VI, have much larger osteocyte lacunae [14, 19, 70]. It should be noted that these results must be interpreted with caution since osteocyte lacunae are three-dimensional structures, while an OLS analysis investigates only 2D sections through the sample. This might lead to an underestimation of the real osteocyte body size due to projection effects. However, we evaluated a large number of bone samples, and the two-way ANOVA analysis revealed a significant reduction of about 14% in OLS-area and 8% in OLS-perimeter of *Ifitm5/*BRIL p.S42L mutants versus WT at both ages. This observation suggests either that osteocyte lacunae are intrinsically smaller or that the unmineralized perilacunar space is narrower. During osteocytogenesis, i.e., during differentiation of a cuboidal osteoblast to an osteocyte, the cell volume normally shrinks to about 70% and it might be that dysregulated OI osteocytes shrink to a larger extent [38, 76]. A further possibility is that the distance between the mineralized matrix and the unmineralized cell membrane, thus the pericellular space, is narrower in *Ifitm5/*BRIL p.S42L. Recently, it was demonstrated that mineralization starts at some distance from the osteocyte cell body and the canaliculi and gradually moves towards the cell, raising the possibility that the remaining unmineralized zone around osteocyte bodies and along canaliculi is smaller in *Ifitm5/*BRIL p.S42L than in WT [77]. In fact, both assumptions are in accordance with the concept that osteocytes in OI have abnormalities in expression of genes regulating dendrite formation, extracellular matrix organization and mineralization [38]. Hence, a further phenotypic observation in *Ifitm5/*BRIL p.S42L, reminiscent of OI [37], is the architecture of the disordered collagen matrix by second harmonic generation microscopy in conjunction with the osteocyte lacuno-canalicular network visualized by a combination of rhodamine staining and confocal laser scanning microscopy on the identical bone surfaces [44, 78]. To our knowledge, the architecture of the osteocyte lacuno-canalicular network has not yet been characterized in OI, although it is widely recognized that a functional intact osteocyte lacuno-canalicular network plays a crucial role in mechanosensation, load adaptation and conversely might be profoundly altered in ageing and diseases [39, 78, 79]. The mean canalicular density in our WT mice showed significant age variation (351.9 and 364.7 m/mm^{3,} at 4- and 8 weeks, respectively) and was about 30% higher than reported earlier in skeletal mature mice (26 weeks: 270 m/mm^3 [39]). This would indicate that bone from young growing mice have higher osteocyte canalicular density than adult mice, which is in agreement with previous observations that the overall canalicular density decreases with age [78–80]. We further observed an age-related increase in the number of cell processes per osteocyte in WT and *Ifitm5/*BRIL p.S42L, which is also in line with previous studies reporting osteocyte canalicular number increase in young mice in parallel to mechanical adaptation during growth [80, 81]. *Ifitm5/*BRIL p.S42L bone showed lower canalicular density than WT. Interestingly, despite increased osteocyte lacunae density in *Ifitm*5/BRIL p.S42L, the number of canaliculi per osteocyte was similar between the two genotypes. A higher density of osteocytes also implies a shorter distance between lacunae which could perhaps explain the overall shorter canalicular length per unit volume (that is, the canalicular network density).

However, osteocyte lacunae and canalicular network were not homogenously distributed throughout the bone matrix [44]. In particular, cross-sectional murine bone displays lamellar regions, mostly at the periosteal and endocortical surfaces with a rather dense and well connected osteocyte lacunar-canalicular network, as well as regions resembling disordered woven bone with a rather loose network of low connectivity and many vascular channels (Figure 10) [39]. It is known that severe forms of OI are characterized by more woven bone formation at the expenses of ordered lamellar bone deposition, so we hypothesize that a higher proportion of woven bone formation contributes to the OI phenotype in our mouse cohort [37, 82]. Alterations of collagen fibril orientation in OI models were previously also observed in the *Brtl+/−* mice by second harmonic generation and by polarized light microscopy, and they were also deduced from measuring the degree of alignment of the mineral particles by small angle X-ray scattering and from osteocyte lacunae orientation in the *mov13* and *oim* mice [34, 40, 72, 83, 84]. Most importantly, disordered collagen orientation is a hallmark of OI type V, OI type VI and atypical OI type VI bone [8, 9, 14, 20]. In accordance, the evaluation of the second harmonic generation microscopy images revealed that the relative amount of disordered matrix is about 2.5 higher in *Iftm*5/BRIL p.S42L than in WT, representing more than half the total cross-sectional area of the midshaft cortical bone (Figure 9, Supplemental Table). Moreover, this ratio was not age-dependent, indicating that the abnormal collagen fiber arrangement indeed represents a bone tissue characteristic of growing *Ifitm5/*BRIL p.S42L mutants. In this context, it is interesting to remark that numerical simulation suggests that lamellar organization of bone leads to a significant (potentially up to hundred-fold) reduction of bone fragility compared to a homogeneous (non-lamellar) structure [85]. The reason is that the interface between two lamellae effectively hinders crack propagation via efficient energy dissipation mechanisms [86]. While there is no direct proof to date, this suggests that a higher proportion of woven (or at least less lamellar) bone could be a universal contributor to the increased fragility of many forms of OI. Noteworthy, woven bone is also characterized by higher osteocyte density, shorter canalicular length, increased vascularity and increased mineralization density [82, 87]. Finally, it should be noted that although recent studies have shown that the mechanical properties of OI bone seem not to be affected by the elevated osteocyte lacunae density, the diminished osteocyte network organization in *Ifitm5/*BRIL p.S42L along with disorganized matrix might have a major impact on fluid flow, diffusion of ions, hormones and signaling molecules, all factors promoting cellular communication and mechanosensation via the osteocyte lacuno-canalicular network, which ultimately influence the bone material quality [61, 76, 88] .

In summary, the results of this study show that despite the lack of a collagen gene mutation, and the lack of growth and size abnormalities, the female *Ifitm5/*BRIL p.S42L mouse shows major OI-related bone tissue alterations such as elevated matrix mineralization, increased pore and osteocyte number with however decreased canalicular density and highly disordered collagen orientation. Although most bone tissue characteristics were both age- and genotype dependent, the differences between genotypes seemed to decrease with age, suggesting an adaptation during growth, as observed in other mouse models [35]. Bone hypermineralization and collagen organization, which likely are major contributors to the overall bone fragility, were always increased in the *Ifitm5/*BRIL p.S42L mouse independently of age. Additional characterization of *Ifitm5/*BRIL p.S42L bone plus *in vitro* osteoblast studies, conducted in parallel with the investigations of tissue level abnormalities presented here, provide complementary molecular and biochemical insights at the intersection of the BRIL and PEDF pathways (Guterman-Ram *et al.,* manuscript in preparation).

Supplementary Material

Refer to Web version on PubMed Central for supplementary material.

Acknowledgements:

This work was supported by the Austrian Social Health Insurance Fund (OEGK), by the Austrian Social Health Compensation Board (AUVA) and by National Institute of Child Health and Human Development (NICHD/NIH, USA) intramural funds to J.C. Marini (HD000408).

The authors thank Paul Roschger and Andreas Roschger for scientific discussion, Martina Behanova for support of statistical analysis and Petra Keplinger, Phaedra Messmer and Sonja Lueger for technical support.

References:

[1]. Forlino A, Cabral WA, Barnes AM, Marini JC. New perspectives on osteogenesis imperfecta. Nat Rev Endocrinol 2011;7: 540–57. [PubMed: 21670757]

[2]. Forlino A, Marini JC. Osteogenesis imperfecta. Lancet 2016;387: 1657–71. [PubMed: 26542481]

[3]. Sillence DO, Senn A, Danks DM. Genetic heterogeneity in osteogenesis imperfecta. J Med Genet 1979;16: 101–16. [PubMed: 458828]

[4]. Willing MC, Pruchno CJ, Atkinson M, Byers PH. Osteogenesis imperfecta type I is commonly due to a COL1A1 null allele of type I collagen. Am J Hum Genet 1992;51: 508–15. [PubMed: 1353940]

[5]. Prockop DJ, Constantinou CD, Dombrowski KE, Hojima Y, Kadler KE, Kuivaniemi H, Tromp G, Vogel BE. Type I procollagen: the gene-protein system that harbors most of the mutations causing osteogenesis imperfecta and probably more common heritable disorders of connective tissue. Am J Med Genet 1989;34: 60–7. [PubMed: 2683782]

[6]. Tauer JT, Robinson ME, Rauch F. Osteogenesis Imperfecta: New Perspectives From Clinical and Translational Research. JBMR Plus 2019;3: e10174.

[7]. Jovanovic M, Guterman-Ram G, Marini JC. Osteogenesis Imperfecta: Mechanisms and signaling pathways connecting classical and rare OI types. Endocr Rev 2021.

[8]. Glorieux FH, Rauch F, Plotkin H, Ward L, Travers R, Roughley P, Lalic L, Glorieux DF, Fassier F, Bishop NJ. Type V osteogenesis imperfecta: a new form of brittle bone disease. J Bone Miner Res 2000;15: 1650–8. [PubMed: 10976985]

[9]. Glorieux FH, Ward LM, Rauch F, Lalic L, Roughley PJ, Travers R. Osteogenesis imperfecta type VI: a form of brittle bone disease with a mineralization defect. J Bone Miner Res 2002;17: 30–8. [PubMed: 11771667]

[10]. Semler O, Garbes L, Keupp K, Swan D, Zimmermann K, Becker J, Iden S, Wirth B, Eysel P, Koerber F, Schoenau E, Bohlander SK, Wollnik B, Netzer C. A mutation in the 5’-UTR of IFITM5 creates an in-frame start codon and causes autosomal-dominant osteogenesis imperfecta type V with hyperplastic callus. Am J Hum Genet 2012;91: 349–57. [PubMed: 22863195]

[11]. Cho TJ, Lee KE, Lee SK, Song SJ, Kim KJ, Jeon D, Lee G, Kim HN, Lee HR, Eom HH, Lee ZH, Kim OH, Park WY, Park SS, Ikegawa S, Yoo WJ, Choi IH, Kim JW. A single recurrent mutation in the 5’-UTR of IFITM5 causes osteogenesis imperfecta type V. Am J Hum Genet 2012;91: 343–8. [PubMed: 22863190]

[12]. Cheung MS, Glorieux FH, Rauch F. Natural history of hyperplastic callus formation in osteogenesis imperfecta type V. J Bone Miner Res 2007;22: 1181–6. [PubMed: 17451374]

[13]. Rauch F, Moffatt P, Cheung M, Roughley P, Lalic L, Lund AM, Ramirez N, Fahiminiya S, Majewski J, Glorieux FH. Osteogenesis imperfecta type V: marked phenotypic variability despite the presence of the IFITM5 c.−14C>T mutation in all patients. J Med Genet 2013;50: 21–4. [PubMed: 23240094]

[14]. Blouin S, Fratzl-Zelman N, Glorieux FH, Roschger P, Klaushofer K, Marini JC, Rauch F. Hypermineralization and High Osteocyte Lacunar Density in Osteogenesis Imperfecta Type V Bone Indicate Exuberant Primary Bone Formation. J Bone Miner Res 2017;32: 1884–1892. [PubMed: 28548288]

[15]. Homan EP, Rauch F, Grafe I, Lietman C, Doll JA, Dawson B, Bertin T, Napierala D, Morello R, Gibbs R, White L, Miki R, Cohn DH, Crawford S, Travers R, Glorieux FH, Lee B. Mutations in SERPINF1 cause osteogenesis imperfecta type VI. J Bone Miner Res 2011;26: 2798–803. [PubMed: 21826736]

[16]. Becker J, Semler O, Gilissen C, Li Y, Bolz HJ, Giunta C, Bergmann C, Rohrbach M, Koerber F, Zimmermann K, de Vries P, Wirth B, Schoenau E, Wollnik B, Veltman JA, Hoischen A, Netzer C. Exome sequencing identifies truncating mutations in human SERPINF1 in autosomal-recessive osteogenesis imperfecta. Am J Hum Genet 2011;88: 362–71. [PubMed: 21353196]

[17]. Venturi G, Gandini A, Monti E, Dalle Carbonare L, Corradi M, Vincenzi M, Valenti MT, Valli M, Pelilli E, Boner A, Mottes M, Antoniazzi F. Lack of expression of SERPINF1, the gene coding for pigment epithelium-derived factor, causes progressively deforming osteogenesis imperfecta with normal type I collagen. J Bone Miner Res 2012;27: 723–8. [PubMed: 22113968]

[18]. Marini JC, Forlino A, Bachinger HP, Bishop NJ, Byers PH, Paepe A, Fassier F, Fratzl-Zelman N, Kozloff KM, Krakow D, Montpetit K, Semler O. Osteogenesis imperfecta. Nat Rev Dis Primers 2017;3: 17052. [PubMed: 28820180]

[19]. Fratzl-Zelman N, Schmidt I, Roschger P, Roschger A, Glorieux FH, Klaushofer K, Wagermaier W, Rauch F, Fratzl P. Unique micro- and nano-scale mineralization pattern of human osteogenesis imperfecta type VI bone. Bone 2015;73: 233–41. [PubMed: 25554599]

[20]. Farber CR, Reich A, Barnes AM, Becerra P, Rauch F, Cabral WA, Bae A, Quinlan A, Glorieux FH, Clemens TL, Marini JC. A novel IFITM5 mutation in severe atypical osteogenesis imperfecta type VI impairs osteoblast production of pigment epithelium-derived factor. J Bone Miner Res 2014;29: 1402–11. [PubMed: 24519609]

[21]. Reich A, Bae AS, Barnes AM, Cabral WA, Hinek A, Stimec J, Hill SC, Chitayat D, Marini JC. Type V OI primary osteoblasts display increased mineralization despite decreased COL1A1 expression. J Clin Endocrinol Metab 2015;100: E325–32. [PubMed: 25387264]

[22]. Kang H, Aryal ACS, Marini JC. Osteogenesis imperfecta: new genes reveal novel mechanisms in bone dysplasia. Transl Res 2017;181: 27–48. [PubMed: 27914223]

[23]. Lindsay SE, Nicol LE, Gamayo AC, Raney EM. An Unusual Presentation of Osteogenesis Imperfecta: A Case Report. JBJS Case Connect 2021;11.

[24]. Grebennikova TA, Gavrilova AO, Tiul’pakov AN, Tarbaeva NV, Belaya ZE, Melnichenko GA. First description of a type V osteogenesis imperfecta clinical case with severe skeletal deformities caused by a mutation in P.119C> T in IFITM5 gene in Russia. Osteoporosis and Bone Diseases 2019;22 (2): 32–37.

[25]. Rauch F, Geng Y, Lamplugh L, Hekmatnejad B, Gaumond MH, Penney J, Yamanaka Y, Moffatt P. Crispr-Cas9 engineered osteogenesis imperfecta type V leads to severe skeletal deformities and perinatal lethality in mice. Bone 2018;107: 131–142. [PubMed: 29174564]

[26]. Moffatt P, Gaumond MH, Salois P, Sellin K, Bessette MC, Godin E, de Oliveira PT, Atkins GJ, Nanci A, Thomas G. Bril: a novel bone-specific modulator of mineralization. J Bone Miner Res 2008;23: 1497–508. [PubMed: 18442316]

[27]. Bogan R, Riddle RC, Li Z, Kumar S, Nandal A, Faugere MC, Boskey A, Crawford SE, Clemens TL. A mouse model for human osteogenesis imperfecta type VI. J Bone Miner Res 2013;28: 1531–6. [PubMed: 23413146]

[28]. Kang H, Aryal ACS, Barnes AM, Martin A, David V, Crawford SE, Marini JC. Antagonism between PEDF and TGF-beta contributes to type VI osteogenesis imperfecta bone and vascular pathogenesis. J Bone Miner Res 2022.

[29]. Guterman-Ram G, Stephan C, Kozloff K, Marini JC. New mouse model for atypical type VI osteogenesis imperfecta caused by IFITM5 S40L mutation In: Calcified Tissue International; 2019. p. S29–S30.

[30]. Carriero A, Zimmermann EA, Paluszny A, Tang SY, Bale H, Busse B, Alliston T, Kazakia G, Ritchie RO, Shefelbine SJ. How tough is brittle bone? Investigating osteogenesis imperfecta in mouse bone. J Bone Miner Res 2014;29: 1392–401. [PubMed: 24420672]

[31]. Fratzl-Zelman N, Misof BM, Klaushofer K, Roschger P. Bone mass and mineralization in osteogenesis imperfecta. Wien Med Wochenschr 2015;165: 271–7. [PubMed: 26208477]

[32]. Wagermaier W, Klaushofer K, Fratzl P. Fragility of Bone Material Controlled by Internal Interfaces. Calcif Tissue Int 2015;97: 201–12. [PubMed: 25772807]

[33]. Bishop N. Bone Material Properties in Osteogenesis Imperfecta. J Bone Miner Res 2016;31: 699–708. [PubMed: 26987995]

[34]. Blouin S, Fratzl-Zelman N, Roschger A, Cabral WA, Klaushofer K, Marini JC, Fratzl P, Roschger P. Cortical bone properties in the Brtl/+ mouse model of Osteogenesis imperfecta as evidenced by acoustic transmission microscopy. J Mech Behav Biomed Mater 2019;90: 125–132. [PubMed: 30366302]

[35]. Kozloff KM, Carden A, Bergwitz C, Forlino A, Uveges TE, Morris MD, Marini JC, Goldstein SA. Brittle IV mouse model for osteogenesis imperfecta IV demonstrates postpubertal adaptations to improve whole bone strength. J Bone Miner Res 2004;19: 614–22. [PubMed: 15005849]

[36]. Glatt V, Canalis E, Stadmeyer L, Bouxsein ML. Age-related changes in trabecular architecture differ in female and male C57BL/6J mice. J Bone Miner Res 2007;22: 1197–207. [PubMed: 17488199]

[37]. Shapiro F, Maguire K, Swami S, Zhu H, Flynn E, Wang J, Wu JY. Histopathology of osteogenesis imperfecta bone. Supramolecular assessment of cells and matrices in the context of woven and lamellar bone formation using light, polarization and ultrastructural microscopy. Bone Rep 2021;14: 100734.

[38]. Zimmerman SM, Dimori M, Heard-Lipsmeyer ME, Morello R. The Osteocyte Transcriptome Is Extensively Dysregulated in Mouse Models of Osteogenesis Imperfecta. JBMR Plus 2019;3: e10171.

[39]. van Tol AF, Schemenz V, Wagermaier W, Roschger A, Razi H, Vitienes I, Fratzl P, Willie BM, Weinkamer R. The mechanoresponse of bone is closely related to the osteocyte lacunocanalicular network architecture. Proc Natl Acad Sci U S A 2020;117: 32251–32259. [PubMed: 33288694]

[40]. Carriero A, Doube M, Vogt M, Busse B, Zustin J, Levchuk A, Schneider P, Muller R, Shefelbine SJ. Altered lacunar and vascular porosity in osteogenesis imperfecta mouse bone as revealed by synchrotron tomography contributes to bone fragility. Bone 2014;61: 116–24. [PubMed: 24373921]

[41]. Fratzl-Zelman N, Morello R, Lee B, Rauch F, Glorieux FH, Misof BM, Klaushofer K, Roschger P. CRTAP deficiency leads to abnormally high bone matrix mineralization in a murine model and in children with osteogenesis imperfecta type VII. Bone 2010;46: 820–6. [PubMed: 19895918]

[42]. Fratzl-Zelman N, Bachinger HP, Vranka JA, Roschger P, Klaushofer K, Rauch F. Bone matrix hypermineralization in prolyl-3 hydroxylase 1 deficient mice. Bone 2016;85: 15–22. [PubMed: 26808442]

[43]. Repp F, Kollmannsberger P, Roschger A, Kerschnitzki M, Berzlanovich A, Gruber GM, Roschger P, Wagermaier W, Weinkamer R. Spatial heterogeneity in the canalicular density of the osteocyte network in human osteons. Bone Rep 2017;6: 101–108. [PubMed: 28377989]

[44]. Kerschnitzki M, Wagermaier W, Roschger P, Seto J, Shahar R, Duda GN, Mundlos S, Fratzl P. The organization of the osteocyte network mirrors the extracellular matrix orientation in bone. J Struct Biol 2011;173: 303–11. [PubMed: 21081167]

[45]. Kerschnitzki M, Kollmannsberger P, Burghammer M, Duda GN, Weinkamer R, Wagermaier W, Fratzl P. Architecture of the osteocyte network correlates with bone material quality. J Bone Miner Res 2013;28: 1837–45. [PubMed: 23494896]

[46]. Roschger P, Paschalis EP, Fratzl P, Klaushofer K. Bone mineralization density distribution in health and disease. Bone 2008;42: 456–66. [PubMed: 18096457]

[47]. Muller R, Van Campenhout H, Van Damme B, Van Der Perre G, Dequeker J, Hildebrand T, Ruegsegger P. Morphometric analysis of human bone biopsies: a quantitative structural comparison of histological sections and micro-computed tomography. Bone 1998;23: 59–66. [PubMed: 9662131]

[48]. Dempster DW, Compston JE, Drezner MK, Glorieux FH, Kanis JA, Malluche H, Meunier PJ, Ott SM, Recker RR, Parfitt AM. Standardized nomenclature, symbols, and units for bone histomorphometry: a 2012 update of the report of the ASBMR Histomorphometry Nomenclature Committee. J Bone Miner Res 2013;28: 2–17. [PubMed: 23197339]

[49]. Schneider CA, Rasband WS, Eliceiri KW. NIH Image to ImageJ: 25 years of image analysis. Nat Methods 2012;9: 671–5. [PubMed: 22930834]

[50]. Bouxsein ML, Boyd SK, Christiansen BA, Guldberg RE, Jepsen KJ, Muller R. Guidelines for assessment of bone microstructure in rodents using micro-computed tomography. J Bone Miner Res 2010;25: 1468–86. [PubMed: 20533309]

[51]. Doube M, Klosowski MM, Arganda-Carreras I, Cordelieres FP, Dougherty RP, Jackson JS, Schmid B, Hutchinson JR, Shefelbine SJ. BoneJ: Free and extensible bone image analysis in ImageJ. Bone 2010;47: 1076–9. [PubMed: 20817052]

[52]. Rao RA, Mehta MR, Leithem S, Toussaint KC, Jr. Quantitative analysis of forward and backward second-harmonic images of collagen fibers using Fourier transform second-harmonic-generation microscopy. Opt Lett 2009;34: 3779–81. [PubMed: 20016611]

[53]. Gauderon R, Lukins PB, Sheppard CJ. Optimization of second-harmonic generation microscopy. Micron 2001;32: 691–700. [PubMed: 11334739]

[54]. Marini JC, Blissett AR. New genes in bone development: what's new in osteogenesis imperfecta. J Clin Endocrinol Metab 2013;98: 3095–103. [PubMed: 23771926]

[55]. Glorieux FH, Travers R, Taylor A, Bowen JR, Rauch F, Norman M, Parfitt AM. Normative data for iliac bone histomorphometry in growing children. Bone 2000;26: 103–9. [PubMed: 10678403]

[56]. Coleman RM, Aguilera L, Quinones L, Lukashova L, Poirier C, Boskey A. Comparison of bone tissue properties in mouse models with collagenous and non-collagenous genetic mutations using FTIRI. Bone 2012;51: 920–8. [PubMed: 22910579]

[57]. Misof BM, Roschger P, Baldini T, Raggio CL, Zraick V, Root L, Boskey AL, Klaushofer K, Fratzl P, Camacho NP. Differential effects of alendronate treatment on bone from growing osteogenesis imperfecta and wild-type mouse. Bone 2005;36: 150–8. [PubMed: 15664013]

[58]. Fratzl-Zelman N, Barnes AM, Weis M, Carter E, Hefferan TE, Perino G, Chang W, Smith PA, Roschger P, Klaushofer K, Glorieux FH, Eyre DR, Raggio C, Rauch F, Marini JC. Non-Lethal Type VIII Osteogenesis Imperfecta Has Elevated Bone Matrix Mineralization. J Clin Endocrinol Metab 2016;101: 3516–25. [PubMed: 27383115]

[59]. Fratzl-Zelman N, Gamsjaeger S, Blouin S, Kocijan R, Plasenzotti P, Rokidi S, Nawrot-Wawrzyniak K, Roetzer K, Uyanik G, Haeusler G, Shane E, Cohen A, Klaushofer K, Paschalis EP, Roschger P, Fratzl P, Zwerina J, Zwettler E. Alterations of bone material properties in adult patients with X-linked hypophosphatemia (XLH). J Struct Biol 2020;211: 107556.

[60]. Granke M, Makowski AJ, Uppuganti S, Nyman JS. Prevalent role of porosity and osteonal area over mineralization heterogeneity in the fracture toughness of human cortical bone. J Biomech 2016;49: 2748–2755. [PubMed: 27344202]

[61]. Albert C, Jameson J, Smith P, Harris G. Reduced diaphyseal strength associated with high intracortical vascular porosity within long bones of children with osteogenesis imperfecta. Bone 2014;66: 121–30. [PubMed: 24928496]

[62]. Miller LM, Little W, Schirmer A, Sheik F, Busa B, Judex S. Accretion of bone quantity and quality in the developing mouse skeleton. J Bone Miner Res 2007;22: 1037–45. [PubMed: 17402847]

[63]. Bortel EL, Duda GN, Mundlos S, Willie BM, Fratzl P, Zaslansky P. Long bone maturation is driven by pore closing: A quantitative tomography investigation of structural formation in young C57BL/6 mice. Acta Biomater 2015;22: 92–102. [PubMed: 25829108]

[64]. Isojima T, Sims NA. Cortical bone development, maintenance and porosity: genetic alterations in humans and mice influencing chondrocytes, osteoclasts, osteoblasts and osteocytes. Cell Mol Life Sci 2021.

[65]. Sadoun E, Reed MJ. Impaired angiogenesis in aging is associated with alterations in vessel density, matrix composition, inflammatory response, and growth factor expression. J Histochem Cytochem 2003;51: 1119–30. [PubMed: 12923237]

[66]. Haffner-Luntzer M, Weber B, Lam C, Fischer V, Lackner I, Ignatius A, Kalbitz M, Marcucio RS, Miclau T. A novel mouse model to study fracture healing of the proximal femur. J Orthop Res 2020;38: 2131–2138. [PubMed: 32232999]

[67]. Sekita A, Matsugaki A, Nakano T. Structural crosstalk between crystallographic anisotropy in bone tissue and vascular network analyzed with a novel visualization method. Materials Transactions 2017;58: 266–277.

[68]. Goring A, Sharma A, Javaheri B, Smith RC, Kanczler JM, Boyde A, Hesse E, Mahajan S, Olsen BR, Pitsillides AA, Schneider P, Oreffo RO, Clarkin CE. Regulation of the Bone Vascular Network is Sexually Dimorphic. J Bone Miner Res 2019;34: 2117–2132. [PubMed: 31269275]

[69]. Callewaert F, Venken K, Kopchick JJ, Torcasio A, van Lenthe GH, Boonen S, Vanderschueren D. Sexual dimorphism in cortical bone size and strength but not density is determined by independent and time-specific actions of sex steroids and IGF-1: evidence from pubertal mouse models. J Bone Miner Res 2010;25: 617–26. [PubMed: 19888832]

[70]. Mahr M, Blouin S, Behanova M, Misof BM, Glorieux FH, Zwerina J, Rauch F, Hartmann MA, Fratzl-Zelman N. Increased Osteocyte Lacunae Density in the Hypermineralized Bone Matrix of Children with Osteogenesis Imperfecta Type I. Int J Mol Sci 2021;22.

[71]. Rauch F, Travers R, Parfitt AM, Glorieux FH. Static and dynamic bone histomorphometry in children with osteogenesis imperfecta. Bone 2000;26: 581–9. [PubMed: 10831929]

[72]. Chipman SD, Sweet HO, McBride DJ Jr., Davisson MT, Marks SC Jr., Shuldiner AR, Wenstrup RJ, Rowe DW, Shapiro JR. Defective pro alpha 2(I) collagen synthesis in a recessive mutation in mice: a model of human osteogenesis imperfecta. Proc Natl Acad Sci U S A 1993;90: 1701–5. [PubMed: 8446583]

[73]. Imbert L, Auregan JC, Pernelle K, Hoc T. Microstructure and compressive mechanical properties of cortical bone in children with osteogenesis imperfecta treated with bisphosphonates compared with healthy children. J Mech Behav Biomed Mater 2015;46: 261–70. [PubMed: 25828157]

[74]. Uveges TE, Collin-Osdoby P, Cabral WA, Ledgard F, Goldberg L, Bergwitz C, Forlino A, Osdoby P, Gronowicz GA, Marini JC. Cellular mechanism of decreased bone in Brtl mouse model of OI: imbalance of decreased osteoblast function and increased osteoclasts and their precursors. J Bone Miner Res 2008;23: 1983–94. [PubMed: 18684089]

[75]. Jandl NM, von Kroge S, Sturznickel J, Baranowsky A, Stockhausen KE, Mushumba H, Beil FT, Puschel K, Amling M, Rolvien T. Large osteocyte lacunae in iliac crest infantile bone are not associated with impaired mineral distribution or signs of osteocytic osteolysis. Bone 2020;135: 115324.

[76]. Dallas SL, Prideaux M, Bonewald LF. The osteocyte: an endocrine cell ... and more. Endocr Rev 2013;34: 658–90. [PubMed: 23612223]

[77]. Ayoubi M, van Tol AF, Weinkamer R, Roschger P, Brugger PC, Berzlanovich A, Bertinetti L, Roschger A, Fratzl P. 3D Interrelationship between Osteocyte Network and Forming Mineral during Human Bone Remodeling. Adv Healthc Mater 2021;10: e2100113.

[78]. Weinkamer R, Kollmannsberger P, Fratzl P. Towards a Connectomic Description of the Osteocyte Lacunocanalicular Network in Bone. Curr Osteoporos Rep 2019;17: 186–194. [PubMed: 31093871]

[79]. Tiede-Lewis LM, Xie Y, Hulbert MA, Campos R, Dallas MR, Dusevich V, Bonewald LF, Dallas SL. Degeneration of the osteocyte network in the C57BL/6 mouse model of aging. Aging (Albany NY) 2017;9: 2190–2208. [PubMed: 29074822]

[80]. Schurman CA, Verbruggen SW, Alliston T. Disrupted osteocyte connectivity and pericellular fluid flow in bone with aging and defective TGF-beta signaling. Proc Natl Acad Sci U S A 2021;118.

[81]. Sugawara Y, Kamioka H, Ishihara Y, Fujisawa N, Kawanabe N, Yamashiro T. The early mouse 3D osteocyte network in the presence and absence of mechanical loading. Bone 2013;52: 189–96. [PubMed: 23044047]

[82]. Shapiro F, Wu JY. Woven bone overview: structural classification based on its integral role in developmental, repair and pathological bone formation throughout vertebrate groups. Eur Cell Mater 2019;38: 137–167. [PubMed: 31571191]

[83]. Fratzl P, Paris O, Klaushofer K, Landis WJ. Bone mineralization in an osteogenesis imperfecta mouse model studied by small-angle x-ray scattering. J Clin Invest 1996;97: 396–402. [PubMed: 8567960]

[84]. Jepsen KJ, Schaffler MB, Kuhn JL, Goulet RW, Bonadio J, Goldstein SA. Type I collagen mutation alters the strength and fatigue behavior of Mov13 cortical tissue. J Biomech 1997;30: 1141–7. [PubMed: 9456382]

[85]. Razi H, Predan J, Fischer FD, Kolednik O, Fratzl P. Damage tolerance of lamellar bone. Bone 2020;130: 115102.

[86]. Peterlik H, Roschger P, Klaushofer K, Fratzl P. From brittle to ductile fracture of bone. Nat Mater 2006;5: 52–5. [PubMed: 16341218]

[87]. Hernandez CJ, Majeska RJ, Schaffler MB. Osteocyte density in woven bone. Bone 2004;35: 1095–9. [PubMed: 15542034]

[88]. Indermaur M, Casari D, Kochetkova T, Peruzzi C, Zimmermann E, Rauch F, Willie B, Michler J, Schwiedrzik J, Zysset P. Compressive strength of iliac bone ECM is not reduced in Osteogenesis Imperfecta and increases with mineralization. J Bone Miner Res 2021.

Highlights:

- *Ifitm5/*BRIL pS42L mice, a model for atypical OI type VI, shows high bone fragility
- Bone material properties were evaluated in mutants and WT at 4 and 8 weeks of age
- Vascularity and osteocyte density decreased with age and were higher in mutants
- Osteocyte canalicular density increased with age and was lower in mutants
- At both ages, mutants show hypermineralization and disordered collagen orientation

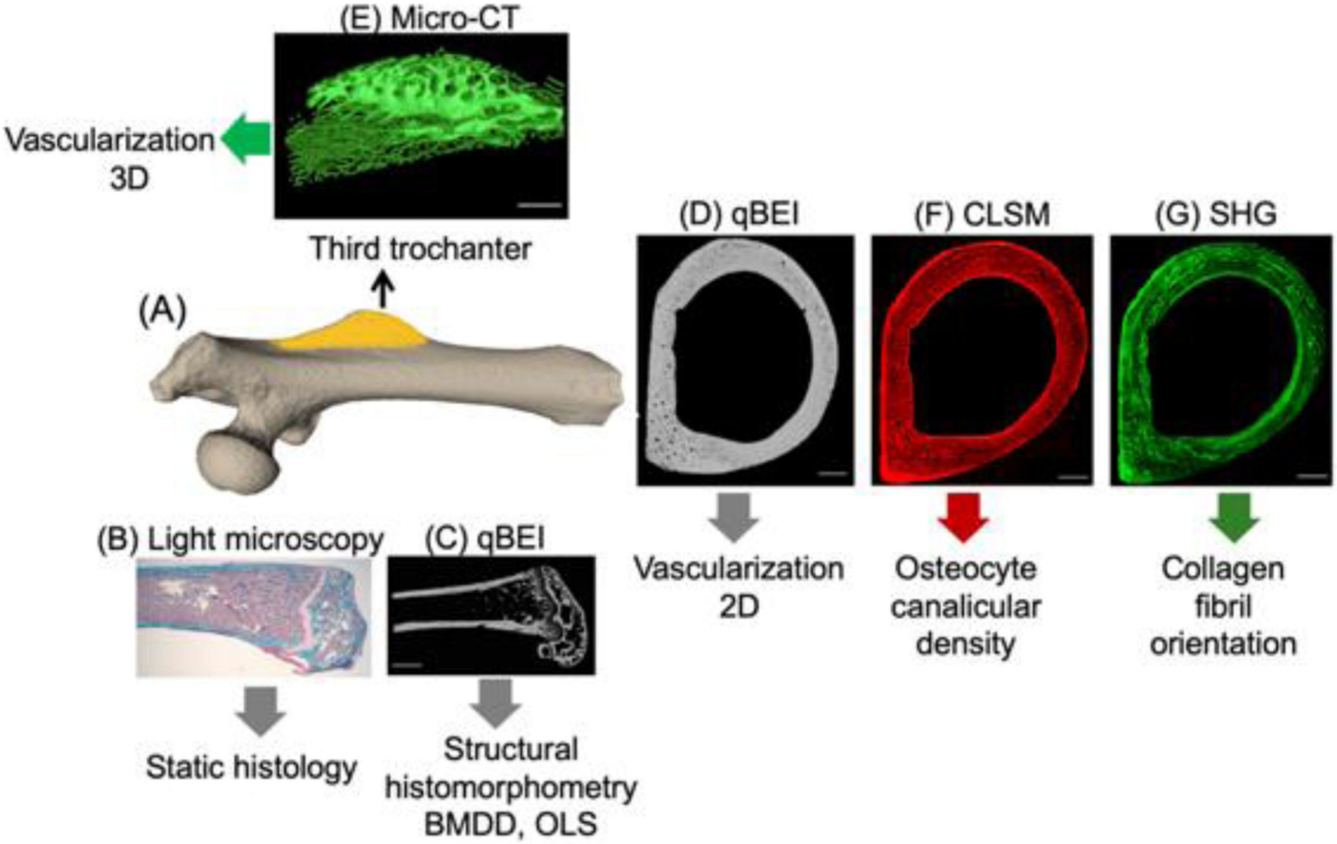

Figure 1:

A Overview of the applied methods for assessing bone material properties. All analyses were performed on the left femur of mice. **B** Light microscopy analysis on the distal part of the femur to examine osteoid deposition (see Figure 4). **C** Quantitative Backscattered Electron Imaging (qBEI) on distal femur to assess the structural indices of bone histomorphometry, the bone mineral density distribution (BMDD), and osteocyte lacunae sections (OLS) (see Figures 3, 5, 6, respectively). **D** Quantitative Backscattered Electron Imaging (qBEI) on midshaft cross section on the proximal part of the femur to assess 2D vascularization (see Figure 8A). **E** Micro-CT analysis from the third trochanter to evaluate 3D vascularization (see Figure 8B). **F** Confocal Laser Scanning Microscopy (CLSM) on midshaft cross sections of rhodamine-stained samples to assess the osteocyte lacuno-canalicular density (see Figure 7). **G** Second Harmonic Generation microscopy (SHG) on midshaft cross section to evaluate collagen fibril orientation (see Figure 9).

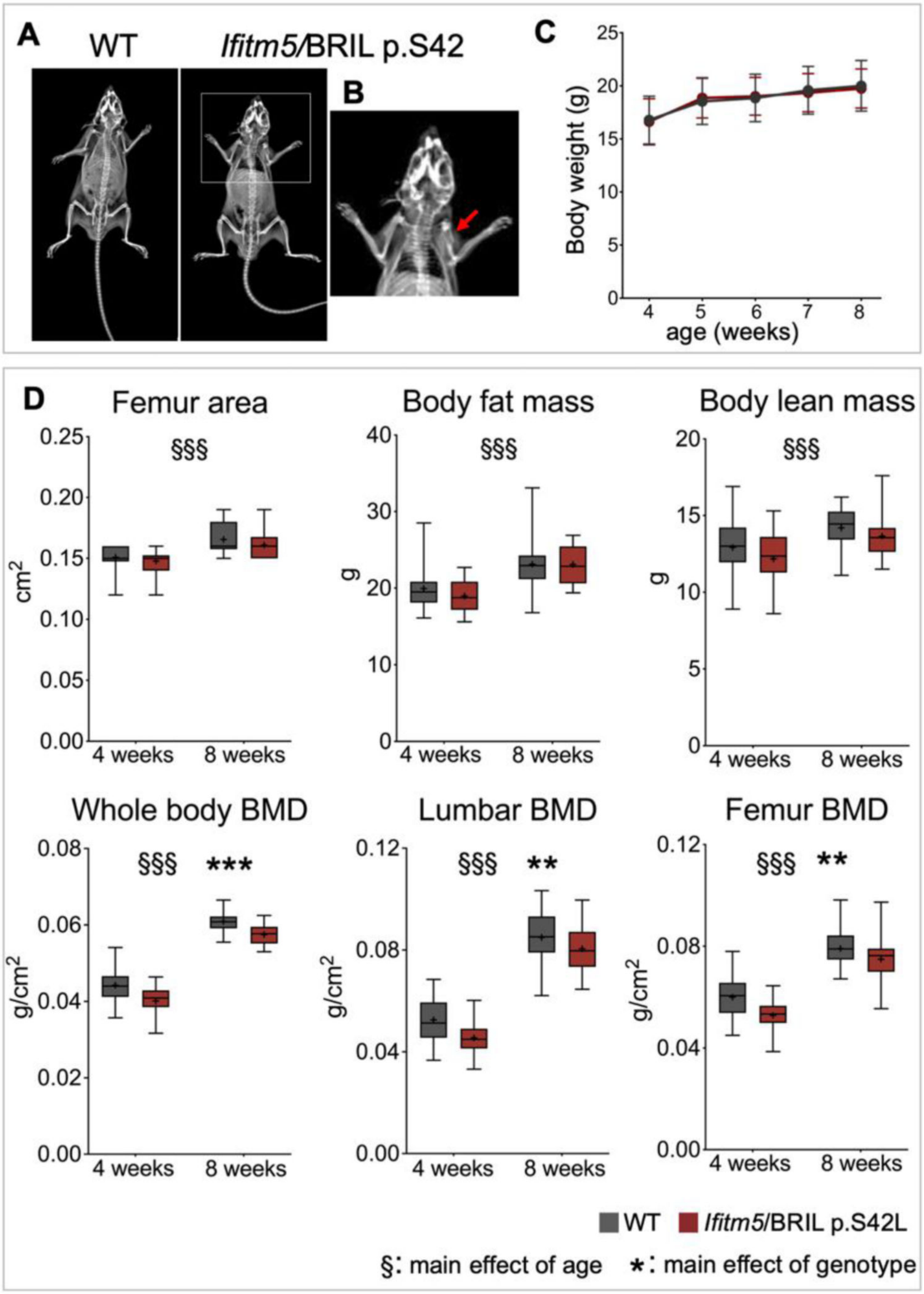

Figure 2:

A, B. Results from X-ray analysis: Representative images of WT (A) and *Ifitm5/*BRIL p.S42 knock-in mice (B) at 8 weeks of age. **B** At larger magnification, a fracture at the humerus can be observed in the *Ifitm5* S42L mouse (red arrow). **C** weight curves from *Ifitm5/*BRIL p.S42 knock-in and WT between 4 and 8 weeks of age **D** Results from DXA analyses: Data are presented as median (25th and 75th percentile), whiskers show the minimum and maximum value, the mean is marked as +; (n=18–26 per group). The mean values (±SD) for each group are compiled in the Supplemental Table. Significant differences based on two-way ANOVA analyses (Table 1) are indicted by the symbols § and * for age and genotype, respectively (with $p < 0.01$ for two symbols and $p < 0.001$ for three symbols).

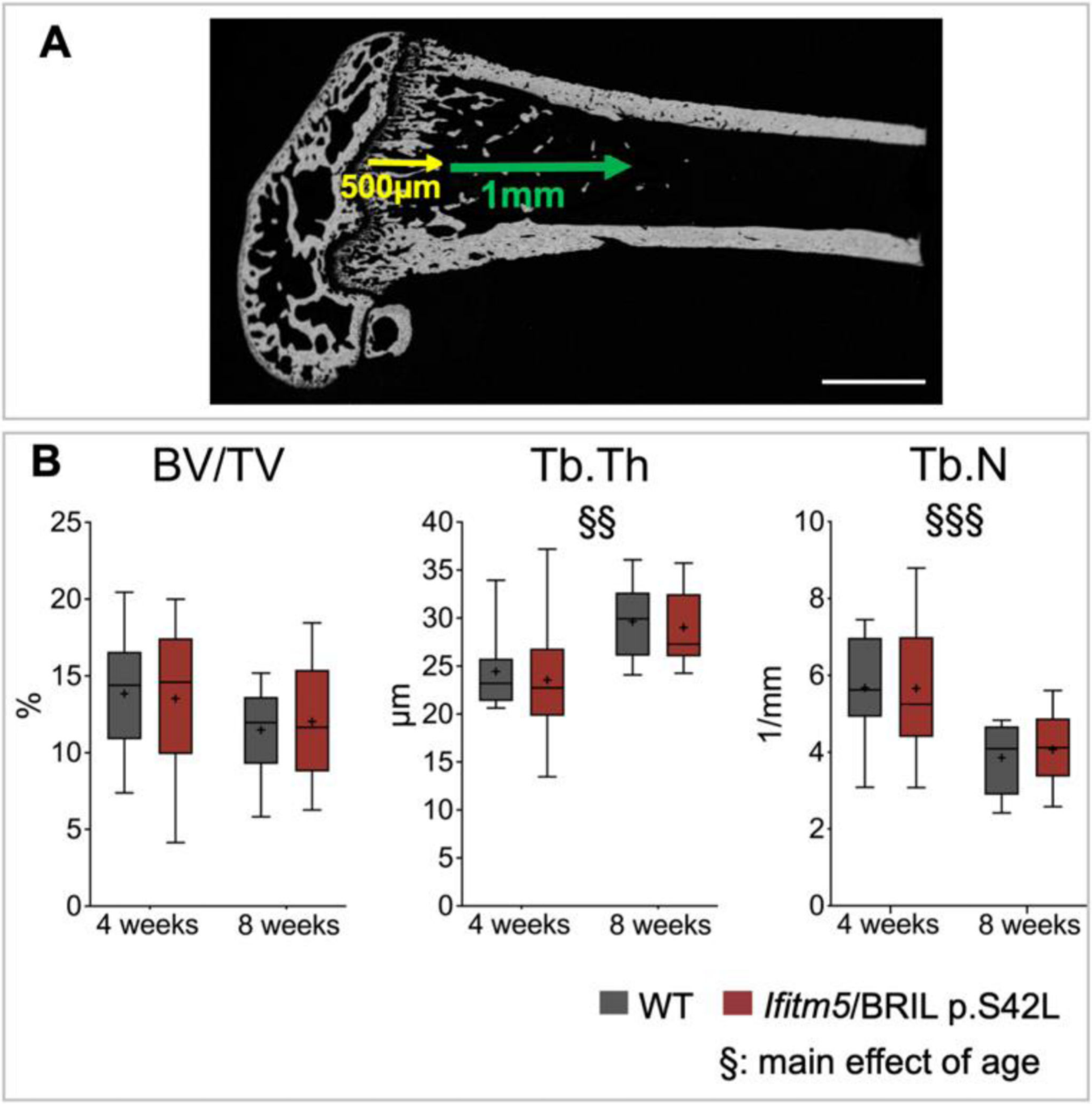

Figure 3:

A Representative quantitative backscattered electron microscopy image of femoral bone showing the region evaluated by qBEI for structural histomorphometry: 1 mm towards the midshaft (green arrow) starting 500 μm below the growth plate (yellow arrow). **B** Results of structural bone histomorphometry: Data in graphs are presented as median (25th and 75th percentile), whiskers show the minimum and maximum value, the mean is marked as +; (n= 9–10 per group). The mean values (±SD) for each group are compiled in the Supplemental

Table. Significant age dependencies based on two-way ANOVA analyses (Table 1) are indicated by § (§§: $p < 0.01$, §§§: $p < 0.001$).

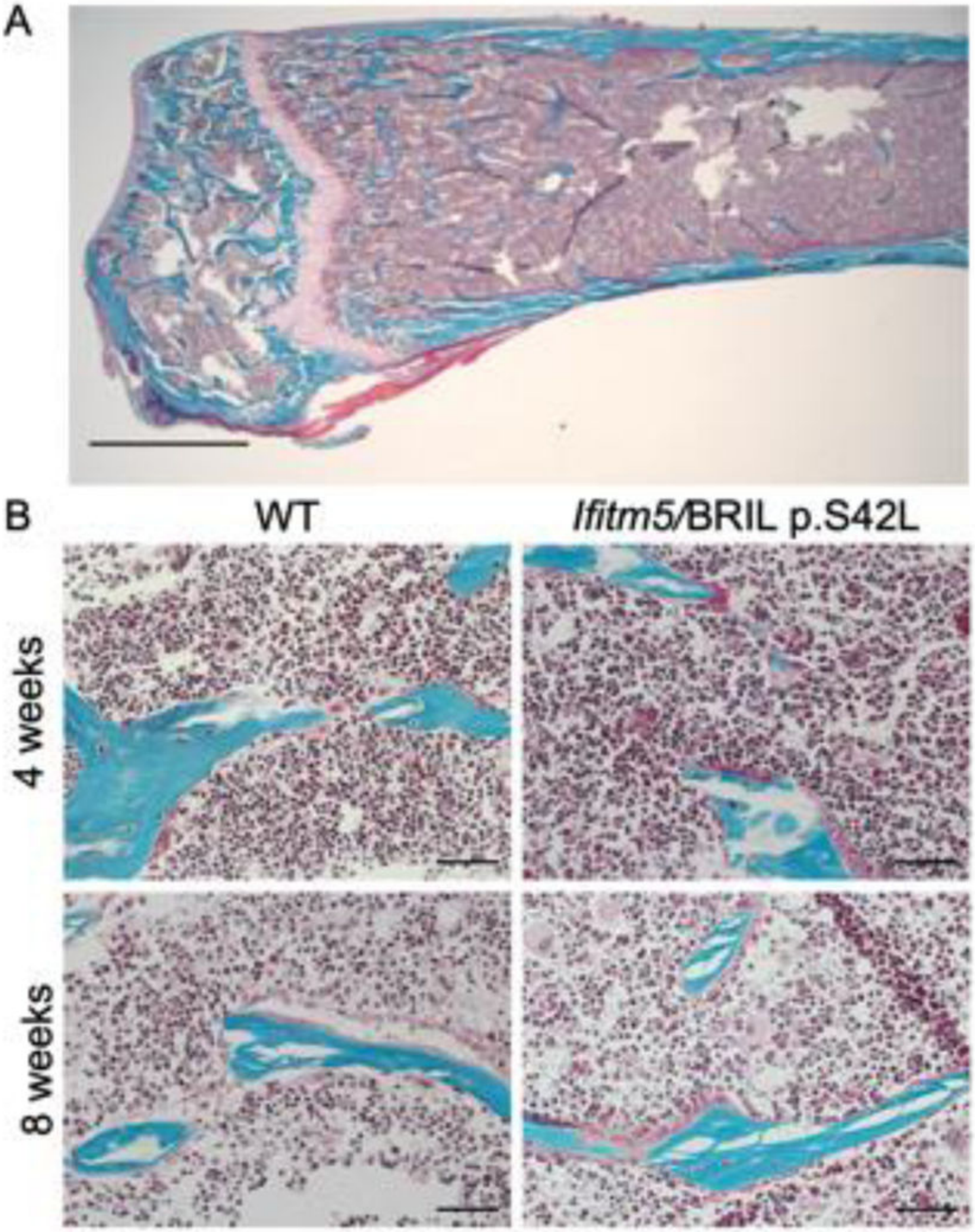

Figure 4:

Light microscopy examinations: **A** representative histological image from a distal femur WT 8-week-old, Goldner trichrome stained (mineralized bone matrix is green, osteoid is red) Scale bar=1mm. **B** Details from femoral bone from WT and *Ifitm5/*BRIL p.S42L at 4 weeks and 8 weeks. Note that no increased osteoid formation is viewed in *Ifitm5/*BRIL p.S42L compared to WT. Scale bar=50 μm.

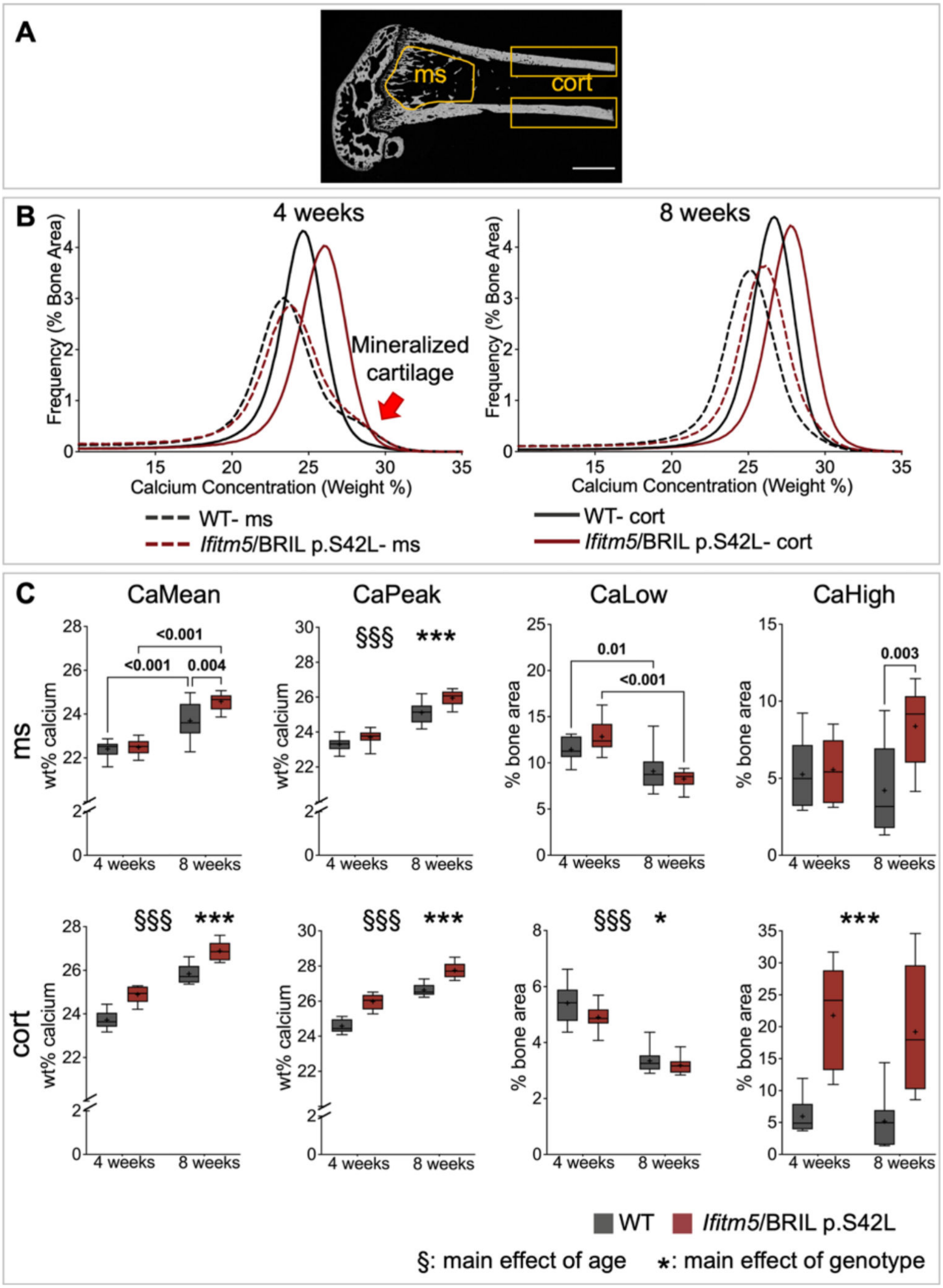

Figure 5:

A Representative quantitative backscattered electron microscopy image of femoral bone illustrating the two investigated regions of interest for bone mineralization density distribution (BMDD) (metaphysis: ms, cortical bone: cort); Scalebar = 1 mm. **B** BMDD curves of metaphyseal and cortical bone from WT and *Ifitm5/*BRIL p.S42L mice (at 4- and at 8-weeks). It can be observed that for both genotypes and at both ages, the BMDD curves of cortical bone (full lines) are shifted to the right, towards higher mineral content of the matrix compared to metaphyseal bone (broken lines). Except for metaphyseal bone at 4 weeks of age, the BMDD curves from *Ifitm5*/BRIL p.S42L are shifted towards higher mineral content of the matrix compared to the corresponding WT curves. The red arrow point towards, a “shoulder” at the right site of the BMDD curve in metaphyseal bone of 4 weeks old WT and *Ifitm5*/BRIL p.S42L, most likely residual mineralized cartilage from the growth plate. The “shoulder” is not anymore present at age of 8 weeks. **C** Significant differences based on two-way ANOVA analyses (Table 1) are indicated by the symbols § and * for age and genotype, respectively (with $p < 0.05$ for one symbol, $p < 0.01$ for two symbols and $p < 0.001$ for three symbols). For CaMean, CaLow and CaHigh in metaphyseal spongiosa (ms) with significant interaction between age and genotype (Table 1), p-values of pairwise comparisons (post-hoc tests) are indicated (when $p < 0.05$). CaMean and CaPeak increased with age, in both genotypes, in both regions of interest and were higher in *Ifitm5*/BRIL p.S42L than WT except for CaMean in metaphyseal bone at the age of four weeks. Note that in cortical bone, where no mineralized cartilage was present, CaHigh was increased in *Ifitm5*/BRIL p.S42L versus WT. Data are presented as median (25th and 75th percentile), whiskers show the minimum and maximum value, the mean is marked as +. ms = metaphyseal spongiosa; cort = cortical bone. (n=9–10 per group). The mean values (±SD) for each group are compiled in the Supplemental Table.

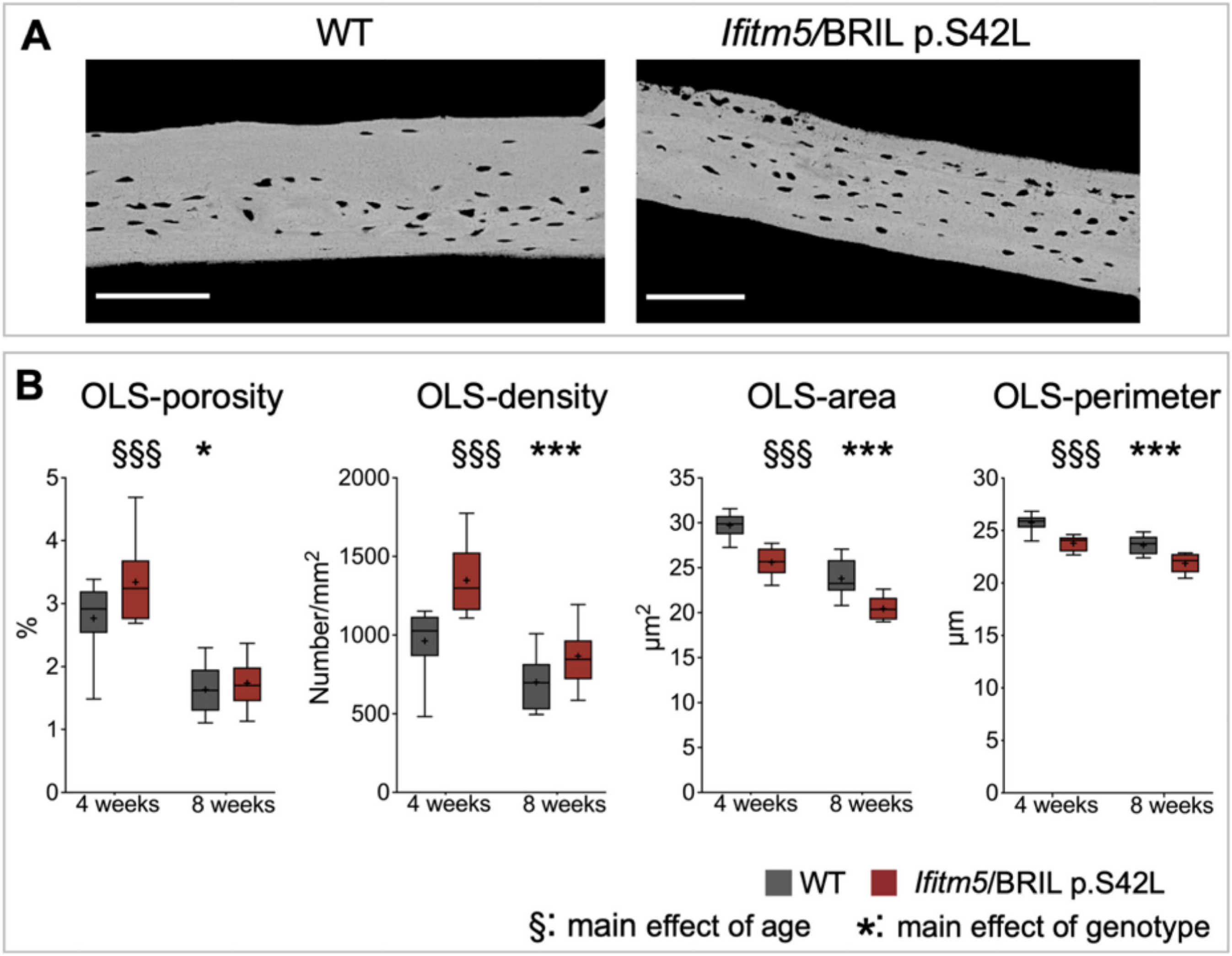

Figure 6:

A Representative quantitative backscattered electron microscopy images of the cortex of femoral bone from 4-weeks old WT and *Ifitm5/*BRIL p.S42L mice. The unmineralized osteocyte lacunae sections (OLS) within the mineralized matrix appear black. Scale bar = 100 µm. **B** Two-Way ANOVA analyses showed for all parameters a significant effect of age and genotype (Table 1). Significant differences are indicated by the symbols § and * for age and genotype, respectively (with $p < 0.05$ for one symbol and $p < 0.001$ for three symbols). Data are presented as median (25th and 75th percentile), whiskers show the minimum and maximum value, the mean is marked as +; (n=9–10 per group). The mean values (±SD) for each group are compiled in the Supplemental Table.

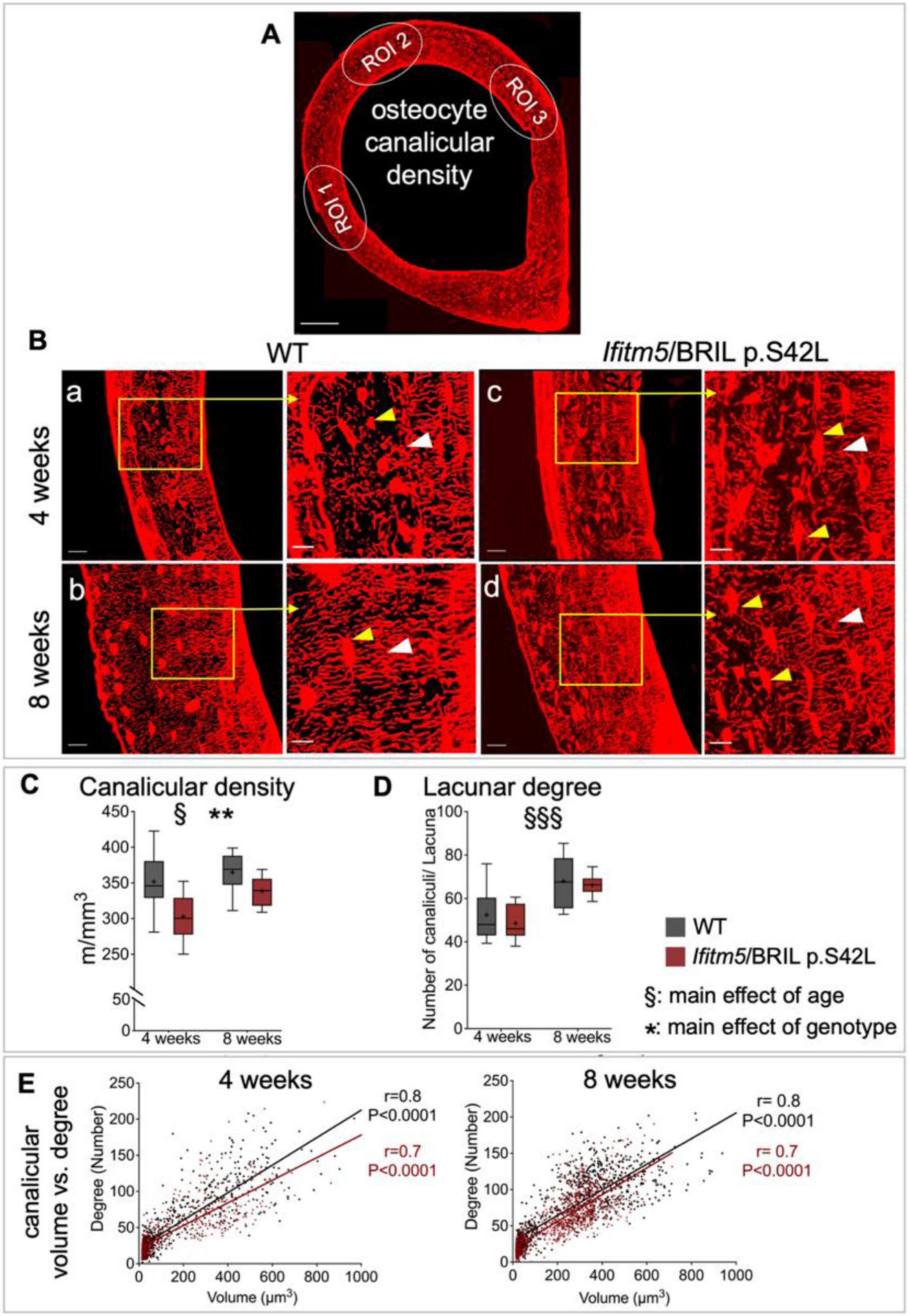

Figure 7:

A Representative confocal laser scanning microscopy (CLSM) imaging of the femoral cross section of the distal femur of a WT 8 weeks old mouse. The overview shows the 3 chosen regions of interest (ROI 1–3); scale bar=200 µm **B** Enlargement of ROI 1 representing rhodamine-stained osteocyte lacunae and canaliculi in WT and *Ifitm5*/BRIL p.S42L mice, Scale bar=20 µm. A looser network with less dense and ordered osteocyte canalicular network can be observed in *Ifitm5*/BRIL p.S42L vs. WT. Osteocyte lacunae (yellow arrow heads), and canaliculi (white arrow heads) are shown in enlarged images of (a, b, c, d); Scale bar=10 µm. **C** Two-way ANOVA analyses (Table 1) showed a significant effect of age and genotype on canalicular density. Significant differences are indicated by the symbols § and * for age and genotype, respectively (with $p < 0.05$ for one symbol and $p < 0.01$ for two symbols): Note that in both genotypes canalicular density increased with age. At both ages, canalicular density was lower in *Ifitm5/*BRIL p.S42L vs. WT. **D** Two-way ANOVA analysis showed that in both genotypes the number of canaliculi per lacuna (degree) increased with age (§§§: $p < 0.001$), whereas there was no significant effect of genotype. **E** Plots showing Pearson correlation between osteocyte lacunae volume and degree, which was similar in both, 4 and 8 weeks of age. Data are presented as median (25th and 75th percentile), whiskers show the minimum and maximum value, the mean is marked as +; (n=8–10). The mean values (±SD) for each group are compiled in the Supplemental Table.

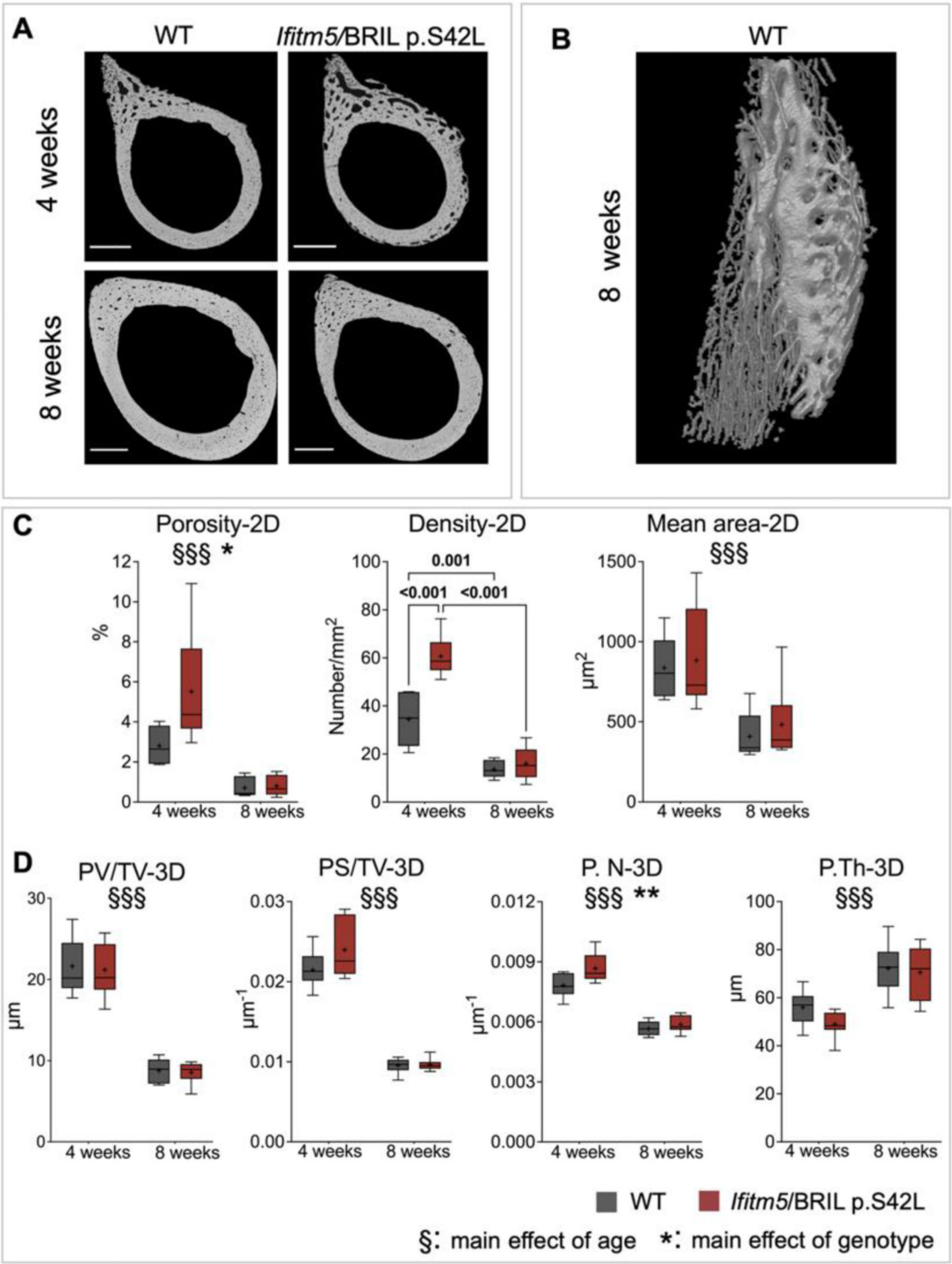

Figure 8:

2D vascularity evaluated by qBEI and 3D vascularity evaluated by micro CT: **A** Representative quantitative backscattered electron microscopy images of femur cross sections of WT and *Ifitm5/*BRIL p.S42L mice (left and right) at 4 and 8 weeks of age (top and bottom, respectively) showing 2D vascular porosity in whole cross-sectional area of the mid-diaphyseal bone, Scale bar=300 µm. **B** 3D rendering of pores at the third trochanter from micro-CT analysis of bone tissue vascularization. **C** The graphs show the results of the 2D-pore evaluations on the cross-sectioned area of cortical bone from two-ANOVA analyses (n=6/group). For both genotypes, porosity, density and mean pore are decreased with age. Significant differences are indicated by the symbols § and * for age and genotype, respectively (with $p < 0.05$ for one symbol, and $p < 0.001$ for three symbols). Note that for Density-2D with significant interaction between age and genotype (Table 1), p-values of pairwise comparisons (post-hoc tests) are indicated (when $p < 0.05$). At both ages, porosity was higher in *Ifitm5/*BRIL p.S42L than in WT. Density was increased in *Ifitm5/*BRIL versus WT at 4 weeks of age, whereas at 8 weeks, this difference was no longer significant. **D** The graphs show the results of 3D micro-CT evaluations of the third trochanter from two-way ANOVA analyses (n=10/group): for both genotypes PV/TV, PS/TV and P.N decreased with age, whereas P.Th increased with age (§§§: $p< 0.001$). At both 4 and 8 weeks of age, P.N was increased in *Ifitm5/*BRIL p.S42L vs. WT (**: $p< 0.01$). There was no effect of genotype for PV/TV, P. Th, PS/TV. All two-way ANOVA results are shown on Table 1. Data are presented as median (25th and 75th percentile), whiskers show the minimum and maximum value, the mean is marked as +. The mean values (±SD) for each group are compiled in the Supplemental Table.

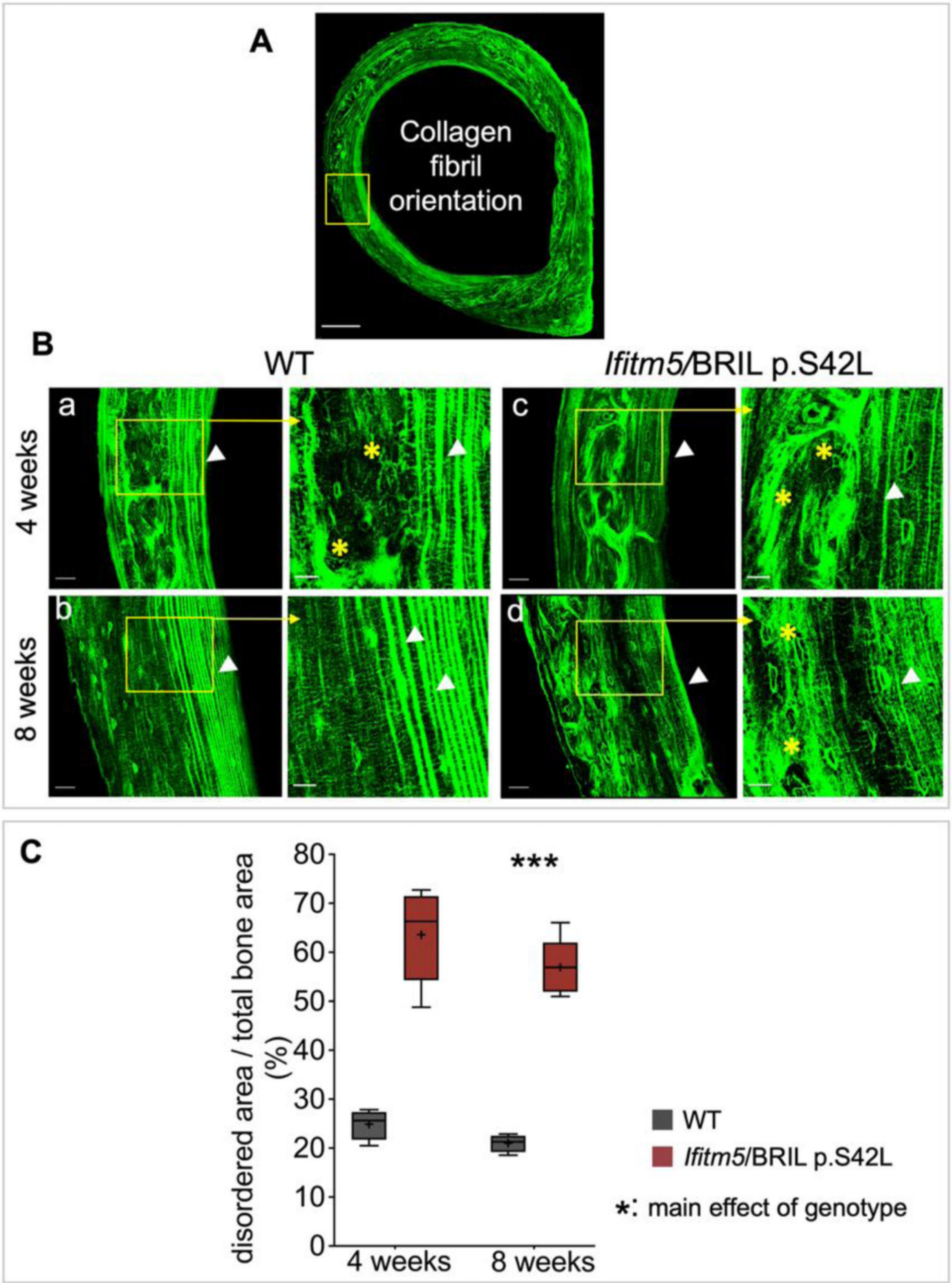

Figure 9:

Second Harmonic Generation (SHG) microscopy analysis of collagen fibril orientation on the total cross-sectional femoral bone area **A** Representative overview image from an 8-week-old WT mouse; scale bar=200 μm. **B** Enlarged images of square area in WT 4 and 8 weeks of age (a and b) and *Ifitm5/*BRIL p.S42L (c and d); scale bar=20 μm. SHG shows areas with ordered collagen fibrils orientation (white arrow heads) in WT mice vs. disordered collagen fibrils orientation (yellow asterisks) in *Ifitm5/*BRIL p.S42L mice. Enlarged images of square in a, b, c, d; scale bar=10 μm. **C** Two-way ANOVA analyses

(Table 1) the proportion of disorganized collagen fibrils was highly increased in *Ifitm5/* BRIL p.S42L versus WT (***: $p < 0.001$) regardless of age. Data are presented as median (25th and 75th percentile), whiskers show the minimum and maximum value, the mean is marked as +. Disordered area = area corresponding to collagen fibrils with highly disordered orientation; (n=4–5/group). The mean values (±SD) for each group are compiled in the Supplemental Table.

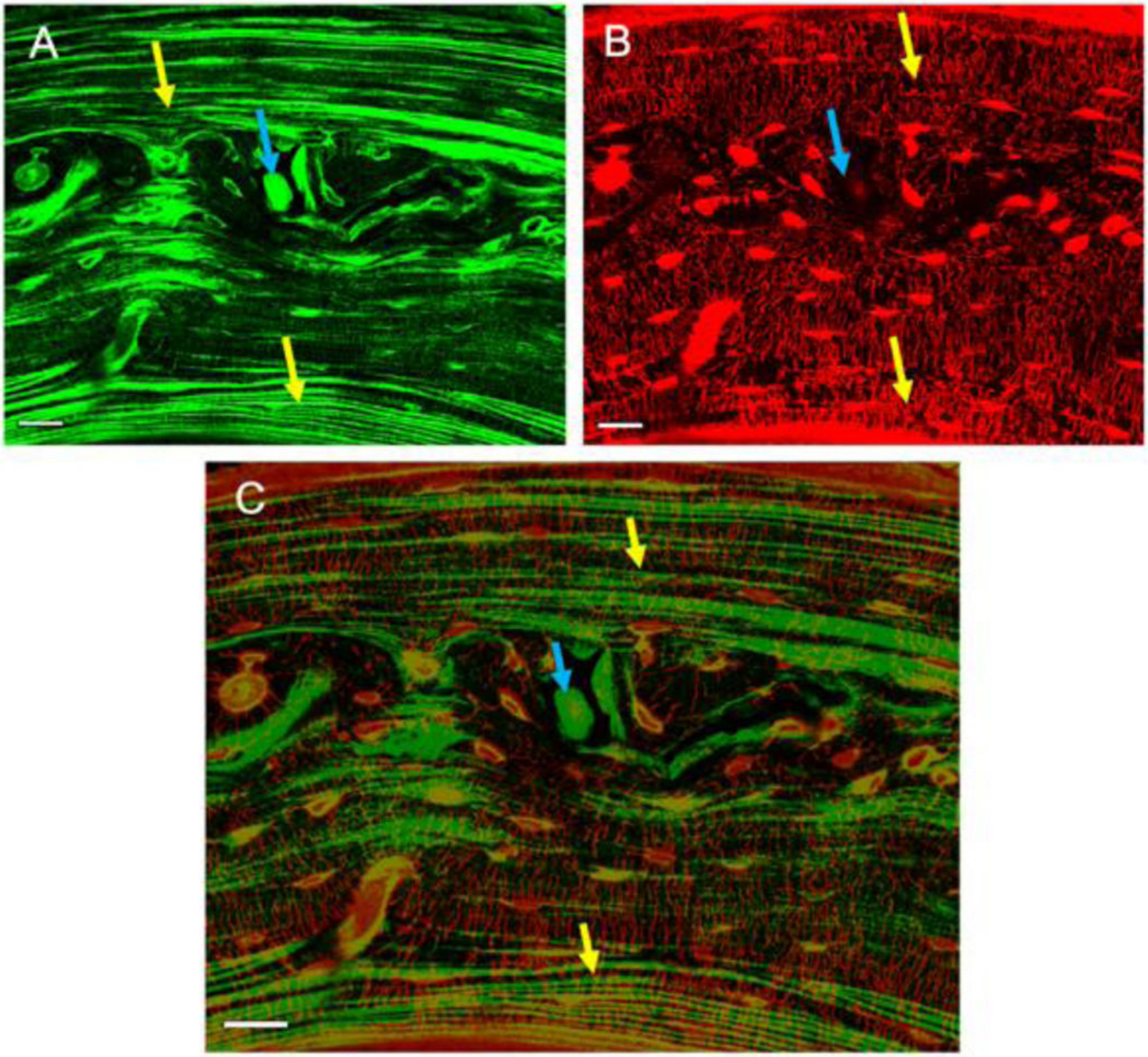

Figure 10:

A Matrix structure of cortical cross-sectional area of the mid-diaphyseal mice femur of a 8-weeks-old WT animal viewed by second harmonic generation (SHG) microscopy. **B** Same surface viewed by confocal laser scanning microscopy (CLSM). **C** Overlay of A and B. The areas with well oriented collagen fibers, lamellar region (yellow arrows) correspond to well-ordered and elongated osteocyte lacuna and canaliculi compared to more round lacunae and less aligned oriented collagen fiber in the middle (blue arrows). The black areas indicate regions with no signal. Scale bar=20μm.

Table 1:

Results of two-way ANOVA analysis

Parameter	Interaction term	Effect of age	Effect of genotype
DXA analysis:			
Femur area (cm^2)	0.731	<**0.0001**	0.11
Body fat mass (g)	0.430	<**0.0001**	0.40
Body lean mass	0.782	**0.0002**	0.07
Whole body BMD (g/cm^2)	0.660	<**0.0001**	<**0.0001**
Femur BMD (g/cm^2)	0.372	<**0.0001**	**0.0011**
Lumbar spine BMD (g/cm^2)	0.508	<**0.0001**	**0.004**
qBEI analysis: bone histomorphometry of structural parameters			
BV/TV (%)	0.738	0.1446	0.935
Tb.N (1/mm)	0.771	**0.0001**	0.802
Tb. Th. (μm)	0.931	**0.0014**	0.627
qBEI analysis: BMDD in metaphyseal bone			
CaMean (Weight% calcium)	**0.023**	<**0.0001**	**0.0081**
CaPeak (Weight % calcium)	0.177	<**0.0001**	**0.0004**
CaWidth (Δ Weight % calcium)	0.902	<**0.0001**	0.4656
CaLow (% bone area)	**0.037**	<**0.0001**	0.5806
CaHigh (% bone area)	**0.0120**	0.2652	**0.0078**
qBEI analysis: BMDD in cortical bone			
CaMean (Weight % calcium)	0.633	<**0.0001**	<**0.0001**
CaPeak (Weight % calcium)	0.290	<**0.0001**	<**0.0001**
CaWidth (Δ Weight % Ca)	0.230	**0.0091**	<**0.0001**
CaLow (% bone area)	0.303	<**0.0001**	**0.0490**
CaHigh (% bone area)	0.681	0.4352	<**0.0001**
qBEI analysis: characteristics of osteocyte lacunae sections (OLS)			
OLS-porosity (%)	0.150	<**0.0001**	**0.041**
OLS-density (Nb. OLS/mm^2)	0.092	<**0.0001**	**0.0001**
OLS-area (μm^2)	0.456	<**0.0001**	<**0.0001**
OLS-perimeter (μm)	0.672	<**0.0001**	<**0.0001**
Confocal laser scanning microscopy analysis: osteocyte canalicular network:			
Canalicular density (m/mm^3)	0.289	**0.029**	**0.0012**
Degree (Nb. of Canaliculi/Lacuna)	0.749	<**0.0001**	0.377
qBEI analysis: 2D vascularity in cortical bone cross-sectional area			
Porosity (%)	0.0540	<**0.0001**	**0.0405**
Density (Number/mm^2)	**0.0018**	<**0.0001**	**0.0003**
Mean area (μm^2)	0.893	**0.0006**	0.5656
Micro-CT analysis: 3D vascularity in the third trochanter			

Parameter	**Interaction term**	**Effect of age**	**Effect of genotype**
PV/TV (%)	0.9012	<**0.0001**	0.681
P. Th (μm)	0.3548	<**0.0001**	0.132
P. N (μm^{-1})	0.0672	<**0.0001**	**0.0036**
P. Sp (μm)	0.7321	<**0.0001**	**0.0048**
PS/TV (μm^{-1})	0.7322	<**0.0001**	0.060
Second harmonic generation microscopy analysis: collagen orientation in the total cortical cross-sectional area			
Relative amount of disordered matrix (% of total bone area)	0.650	0.097	<**0.0001**

Methods and significant values are **bold**